Spring 2019

# Multifunctional Microgels for Nanoparticle-Based Detection Methodologies

Alyson Silva
*Western Washington University*, alysonking44@gmail.com

# MULTIFUNCTIONAL MICROGELS FOR NANOPARTICLE-BASED DETECTION METHODOLOGIES

By

Alyson Dee Silva

Accepted in Partial Completion
of the Requirements for the Degree
Master of Science

ADVISORY COMMITTEE

Chair, Dr. Steven R. Emory

Dr. David A. Rider

Dr. Ying Bao

GRADUATE SCHOOL

Kathleen L. Kitto, Acting Dean

**Master's Thesis**

In presenting this thesis in partial fulfillment of the requirements for a master's degree at Western Washington University, I grant to Western Washington University the non-exclusive royalty-free right to archive, reproduce, distribute, and display the thesis in any and all forms, including electronic format, via any digital library mechanisms maintained by WWU.

I represent and warrant this is my original work, and does not infringe or violate any rights of others. I warrant that I have obtained written permissions from the owner of any third party copyrighted material included in these files.

I acknowledge that I retain ownership rights to the copyright of this work, including but not limited to the right to use all or part of this work in future works, such as articles or books.

Library users are granted permission for individual, research and non-commercial reproduction of this work for educational purposes only. Any further digital posting of this document requires specific permission from the author.

Any copying or publication of this thesis for commercial purposes, or for financial gain, is not allowed without my written permission

Signature: Alyson D. Silva

Date: May 28, 2019

# Multifunctional Microgels for Nanoparticle-Based Detection Methodologies

A Thesis Presented to
The Faculty of
Western Washington University
In Partial Fulfillment of
The Requirements for the Degree
Master of Science

By
Alyson D. Silva
June 2019

# Abstract

In this study, pH-responsive microgel particles, comprised of 2-vinyl pyridine (P2VP) and styrene (PS), are explored as scaffolds to assemble metallic nanoparticles (NPs) for ultrasensitive detection strategies. Microgel particles serve as size-tunable scaffolds to assemble metal (silver or gold) NPs for surface-enhanced Raman scattering (SERS) vibrational spectroscopy. The high sensitivity of SERS arises from the enormous enhancement of the Raman scattering cross sections of molecules adsorbed to roughened metal surfaces, such as metal NPs. Using a sterically stabilized latex of random copolymers of PS and P2VP ($PS_xP2VP_y$), this polymer is capable of transitioning to a microgel state through acid-base titration. This effect can be used to manipulate the interparticle spacing between adsorbed metal NPs in order to optimize SERS enhancement. The size of these metal NPs, usually gold or silver (Au NPs or Ag NPs), can also be tuned to further optimize SERS enhancement. These microgel-NP composites are characterized and their pH-responsive behavior is demonstrated to be reversible in both bulk SERS and single-particle SERS analyses.

# Acknowledgements


## Research Advisor

Dr. Steven R. Emory

## Thesis Committee Members

Dr. David A. Rider

Dr. Ying Bao

## Western Washington University Chemistry Graduate Program Advisor

Dr. James Vyvyan

## Western Washington University Chemistry Department Chair

Dr. Spencer Anthony-Cahill

## Western Washington University Chemistry Department

Sam Danforth

## Western Washington University Scientific Technical Services

Charles Wandler

Michael Kraft

## Western Washington University Advanced Materials Science and Engineering Center

Kyle Mikkelsen

## Western Washington University Research and Sponsored Programs

## Emory Research Group Members

Sage Olson, Joelle Lo, Ali Pierce, Boomer Lusink

# TABLE OF CONTENTS

# List of Figures

# List of Tables

# Chapter 1: Introduction

## 1.1 Project Overview

New chemical imaging and measurement technologies are needed to help scientists investigate important challenges such as brain function, cancer detection, and discerning between live tumor cells and dormant cells. Surface-enhanced Raman scattering (SERS) has the capability of detecting chemical signal changes due to the electromagnetic field of the bound nanoparticles (NPs) enhancing the Raman signal. The concept of a SERS substrate capable of dynamically tuning SERS-active particle distances is therefore very attractive and is a primary motivation of this work. However, the main issue with such a system, is the tendency for nanoparticles (NPs) to irreversibly aggregate together, which greatly reduces measurement reproducibility. Accordingly, anchoring SERS-active NPs to polymeric substrates has been explored as a method for stabilizing and improving the sensitivity and reproducibility of SERS.[1] Microgels comprised of 2-vinylpyridine (P2VP) have the multifunctionality of pyridine residues throughout a macromolecular network. These P2VP networks allow for polymer solvation and swelling, as well as electrostatic and ligand coordination to metal ions. The study of the synthesis of a sterically-stabilized latex consisting of a random copolymer of polystyrene (PS) and P2VP with divinylbenzene (DVB) crosslinker is thereby described. The dimensions of resulting latex particles and their transitions to a swellable microgel have been studied by acid-base titration and monitored by dynamic light scattering.

The following project, as seen in **Figure 1.1**, involves a size-controlled reduction of silver or gold ions onto gold NPs on the surface of P2VP microgels to fine-tune the size and interparticle distance between the NPs. These SERS signals can therefore be further adjusted by altering the pH of these multifunctional particles via acid-base titrations. These multifunctional microgels will

be characterized via atomic force microscopy (AFM), scanning transmission electron microscopy (STEM), energy-dispersive x-ray spectroscopy (EDS), UV-Vis spectroscopy, bulk SERS, and single-particle SERS.

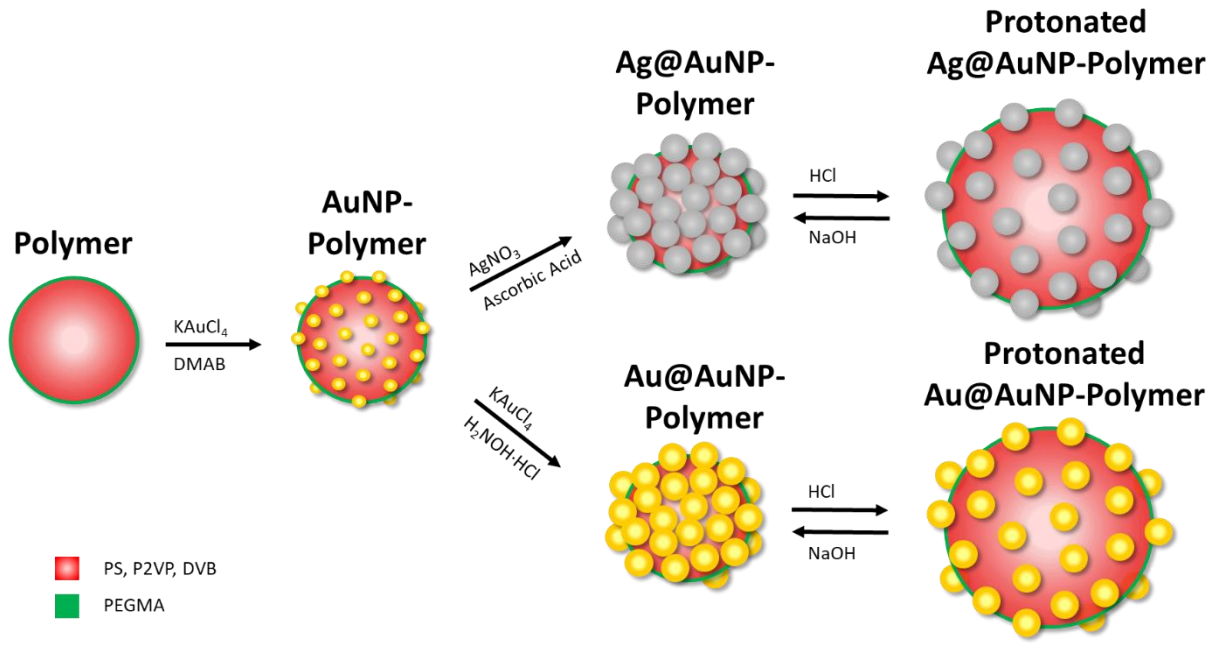


**Figure 1.1**. Generalized mechanism for the formation and reversible transition of multifunctional microgels.

The following thesis describes the importance and functions of these multifunctional microgels through the use of detecting pH changes in a chemical environment.

## 1.2 Sensors

Sensors are highly profitable and sought after within chemical research and industry. Chemical sensors are generally understood to be molecular devices that transform chemical information into analytically useful and reversible signals, such as electrical, electronic, magnetic, or optical signals.[2] These type of sensors contain a receptor, known as a reception site, linked to a

signal source, such as a chromophore, fluorophore, or MRI contrast agent. Binding with a target analyte produces a change in the receptor properties, such as fluorescence, absorption or vibration, for example.[2] An effective sensor also contains a signal transduction element to generate a measurable signal from an analyte-receptor binding event, as well as a device that outputs a result.[3] Cell surface sensors, for example, have the potential to provide rapid sensing of diseases and infections with minimal processing, while the rich environment presented by the cell exterior also gives these sensors the capability to read out the phenotypes of the cells.[3] When developing effective sensors, it is important to take into account the size, shape, surface charge, roughness and hydrophobicity of the nanoparticles being analyzed as well as their role in selective interactions.[3]

Luminescent chemosensors offer the possibility of a sensitive, rapid and reliable determination of a wide range of analytes using simple and cheap instrumentation.[4] CdSe quantum dots (QDs) are frequently used fluorescent semiconductors because size modulation of its band gap enables an accurate tuning of the emission maximum across the visible region. This enables time-gated detection in bioimaging experiments with resistance to photobleaching, which reduces the short-lived fluorescence signal arising from many biomolecules.[4] QDs have some intrinsic value as luminescent sensors because their photophysical properties are not altered by analytes in the surrounding medium, allowing the implementation of a sensing response by combining the acid-sensitive QDs with chemosensitive molecular components to yield peculiar electrochemical and spectroscopic properties.[4] Luminescent sensors can also be obtained through the functionalization of polymers with luminescent tags. Poly(aryleneethynylene)s (PAEs), for example, are conjugated polymers that show absorbance and fluorescence in the visible spectrum.[5] They are easily synthesized and often show exquisitely sensitive changes of fluorescence when exposed to analytes; the sensor binds reversibly to an analyte and detects the presence of the

analyte through the change of a property that can be observed, such as fluorescence (as low as 1-10μM PAE).[5] Recent applications for such pentiptycene-based PPEs are sensing target explosives in land mines.[6,7]

A desired technique for sensing target analytes in biological systems is binding target analytes to transition metal ions and particles. Silver has the highest electrical and thermal conductivity among the metals, giving applications in the electronic industry and photographic and imaging industry.[8] The types of sensors used utilizing silver are coordination based systems, reaction based systems, and others (i.e., QDs, nanoparticles, polymers and oligonucleotides based). In coordination-based systems, silver chemosensors have been developed mainly based on the metal coordination to sulfur containing ligands, which relies on fluorescence detection based on fluorescence quenching rather than enhancement.[8] This type of system is disadvantageous for a high signal output as well as for bioimaging applications. In reaction based systems, kinetically inert metal-ligand complexation requires an external, strong ligand to reverse the binding process which limits the use of such probes for time-dependent monitoring and allows for possible interference from other metal ions (i.e., mercury).[8] However, this reaction-based approach to selectively sense Ag(I) can also be used to detect Ag nanoparticles (Ag NPs) quantitatively, which allows for the application of the simple quantification of Ag NPs in consumer products such as hand sanitizer gel and fabric softener.[9] NP-based sensing systems utilize colorimetric and fluorescent methods for detection of silver ions. Polymer systems exhibit a high selectivity for Ag(I) over most metal ions, including Hg(II) and Pb(II), with reversibility.[10] Likewise, gold nanoparticles (Au NPs) can be modified with a specific ligand to provide them with specific binding selectivity towards Ag(I) in such a way to cause the aggregation of the NPs, leading to a color change.[11,12] Silver detection systems, however, are far away from the reality of application

for bioimaging due to the high concentration of chloride ions inside cells, leading to the precipitation of silver chloride which is toxic.[8]

In recent studies, gold has shown to have the strongest relativistic effect among related transition metal elements.[8] Au NPs below 5 nm in size have been exploited for surface-based chemical reactions.[13] Au NPs below 100 nm in size have received tremendous attention in various fields, including chemistry, biology, and clinical chemistry for their advantageous chemical and photophysical properties that can be readily tuned by surface modifications.[14] Gold-thiol complexes, such as solganol, auranofin and sanocrysin, are representative gold-based drugs for the treatment of several diseases including rheumatoid arthritis, asthma, malaria, HIV, and brain lesions as well as anticancer agents.[15-18] Also, the development of fluorescent probes for gold ions with very high selectivity allows the quantification of gold species in homogeneous samples below the ppb level through the use of fluorimetry with no appreciable interference from other metal species.[8] This allows the application of bioimaging of gold species in living systems as well as gold nanoparticles in living systems. Bajaj *et. al* utilized Au NPs functionalized with a fluorescent polymer [carboxylate poly(*para*-phenyleneethynylene)] to discriminate a series of cell lines through the binding disruption of the Au NP-polymer complex, generating different fluorescence response patterns for each cell line and thus identifying human cancerous, metastatic and normal breast cells.[19] Au NPs have proven to exhibit differential affinity towards various target analytes and thus are extremely useful in real-world applications.

There are various types of chemical sensors that can be used for an assortment of applications. SERS-based techniques utilizing antibodies have been successfully applied to immunoassay-based methodologies.[3] The detection of cancer circulating cells (CTCs) can be accomplished by combining the capturing capability of a magnetic bead and specific labeling of

SERS nanotags, giving rise to the possibility of SERS-based systems for *in vivo* tumor targeting.[20.21] Likewise, targeting carbohydrates has been useful for diagnosis because of the alterations of carbohydrates found on a plasma membrane having correlation with diseases such as liver fibrosis, pancreatic cancer and cervical cancers.[22] These specific recognition-based sensors, however, require pre-identification of the biomarkers and prove limiting when used in systems containing multiple analytes; subtle changes in the biomarker levels may be indicative of dramatic phenotype differences of cancer cells.[3]

## 1.3 Nanoparticle Synthesis

The uses of NPs for various applications can be traced through history for over a thousand years. Paracelsus wrote about the curative properties of "gold quintessence," which he detected by the reduction of gold chloride by vegetable dig-outs in alcohols or oils for the use of healing a number of mental diseases and syphilis.[23] In 1583, alchemist David de Planis-Campy served Louis XIII of France his "longevity elixir," which consisted of a colloidal solution of gold in water.[23] In recent years, however, NPs have been sought after for uses in various scientific studies, such as catalysis, electronics, optics, and environmental and biotechnology.[24] Nanomaterials show unique properties and often times changed physical, chemical and biological properties compared to their macro-scaled counterparts.[25] By altering the physical appearance of these NPs, such as size, shape and surface roughness, the chemical and biological properties of these NPs can be drastically altered to allow them to find use in highly sensitive analytical assessments, ablation thermal and radiotherapy development, and drug and gene delivery.[26-28]

Faraday was the first to recognize that gold salts could be reduced to form ruby colored solutions of "finely divided" gold particles.[29] The usual approach to reducing these metal salts is

through the use of a chemical reduction using a variety of organic and inorganic reducing agents, such as sodium citrate, ascorbate, sodium borohydride, formaldehyde, elemental hydrogen, *N*,*N*-dimethylformamide (DMF), amines, and poly(ethylene glycol)-block copolymers.[24,30-33] For example, reducing silver ions ($Ag^{+}$) leads to the formation of metallic silver ($Ag^{0}$) followed by agglomeration into oligomeric clusters, formulating metallic colloidal silver particles.[34,35] Metal atoms and clusters formed at the early stages of the reaction have short lifetimes and are extremely reactive, and the presence of metallic NPs in a reduction reaction can cause additional nucleation to formulate not only new, smaller NPs but also grown, larger NPs.[36] This technique of fine-tuning the size of NPs has proven desirable for both analytical and biomedical applications and is analyzed in the following project.

Silver NPs (Ag NPs) exhibit inhibitory and bactericidal effects that make them a desired material for bio-applications, but has received a lack in practical application due to potential toxicity of silver cations in a biological system.[24] Gold NPs (Au NPs), on the other hand, are flexible agents with a high surface area to amount ratio that can be readily modified with ligands containing functional groups such as thiols, phosphines and amines, making them highly desirable for biomedical applications.[23,37] Upon illumination, 10 – 200 nm Au NPs can support localized surface plasmon resonances (LSPRs) which are coherently localized oscillations of free conduction band electrons.[38] When the incident light is resonant with the wavelengths of their surface plasmons, the electrons move under the influence of the external field, giving rise to a net change difference at the NP boundaries as seen in **Figure 1.2**.[38] The LSPR wavelength and

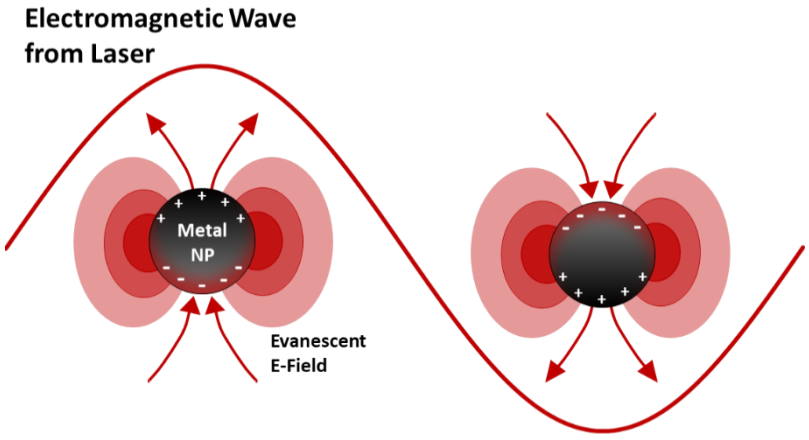


**Figure 1.2**. Schematic of the localized surface plasmon resonance on metal nanoparticles, such as gold or silver. Upon illumination at resonant wavelengths, conduction band electrons on the surface of the nanoparticles are delocalized and undergo collective oscillation.

extinction cross-section of Au NP colloids are size and shape dependent, so by changing the size and shape of the Au NPs the LSPR can be tuned to a desired wavelength to maximize light absorption.[38] This light absorption causes a generation of heat that can be utilized in cancer therapy to damage or destroy cancerous cells and tissues, which is a technique being utilized at Nanospectra Biosciences, Inc. (founded in 2002).[38] This excitation of LSPRs has also proven useful in analytical applications, particularly through the use of Raman scattering.

## 1.4 Raman Spectroscopy

The Raman effect is the inelastic scattering phenomenon that involves a net energy change between the scattered beam and the incident beam used to excite targeted molecules in a sample, first discovered by Sir C.V. Raman in 1928.[39] In elastic scattering, also known as Rayleigh scattering, a molecule in the ground state absorbs energy from an incident beam and excites to a virtual energy level; this excited molecule then releases energy in the form of light at the same wavelength as the incident beam, allowing the molecule to fall back to its original ground state in

energy.[39] In inelastic Raman scattering, however, the scattered radiation and incident radiation have different frequencies with a change in polarizability indicating rotational and vibrational transitions in molecules; a molecule that falls from the virtual state to an energy level above ground state is known as a Stokes vibration while a molecule that falls to an energy level below ground state is known as an Anti-Stokes vibration.[39] These differences in energies can be seen in **Figure 1.3**. The Stokes lines are far more intense than Anti-Stokes lines and can be studied within single-molecules of low temperature solids, room temperature liquids and dielectric surfaces with very small cross sections.[39-41]

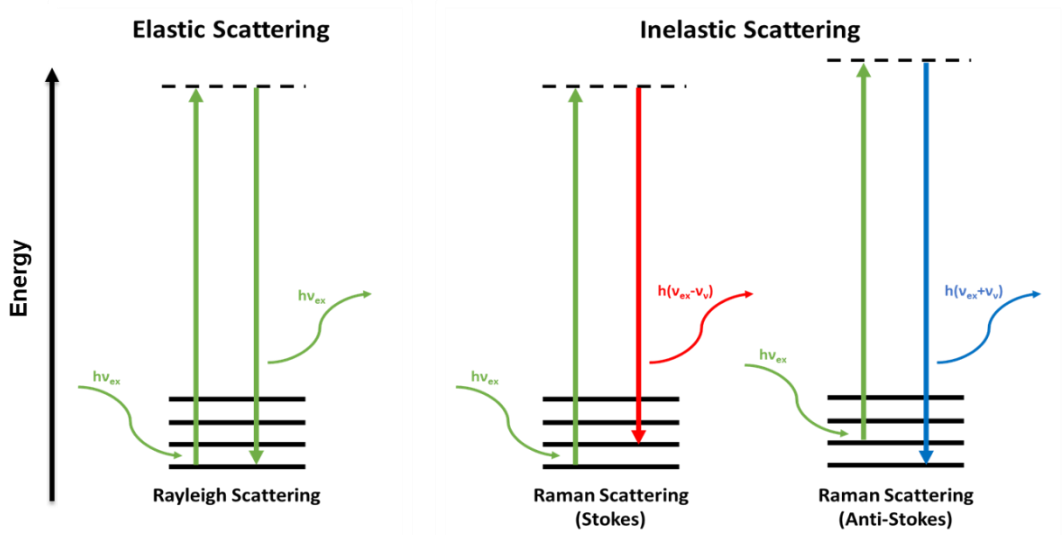


**Figure 1.3**. Schematic diagram of elastic and inelastic scattering processes, where spacing between solid lines corresponds to molecular vibrational energy levels.

A Raman spectrometer requires a monochromatic ion laser source with outputs in the blue or green region of the spectrum to shine into a capillary tube with a liquid or solid sample, or a laser with a higher power and special cells for gases; the detector analyzes the scattered light energies that differ from that of the laser source and allows the digital output to produce high Raman intensities with minimal photodecomposition, fluorescence, and minimal absorption.[39] The

data can provide signal-to-noise considerations where the scattered signal is the analytical signal and fluorescence from any source is the background signal.[39] This type of signal, however, is a very weak signal that cannot provide detailed molecular information due to rapid photobleaching.[40]

## 1.5 Surface-Enhanced Raman Spectroscopy

In 1974, Fleischmann *et. al.* observed a significant enhancement in the typical Raman signal when acquiring a spectrum of pyridine adsorbed onto a roughened silver electrode.[42] It was discovered that this enhancement of signal was due to a combination of electromagnetic enhancement and chemical enhancement. Electromagnetic enhancement involves excitation of the surface plasmons to increase the local field experienced by a molecule (e.g., Rhodamine 6G) adsorbed on the surface of a roughened, metal particle, thereby creating "hot spots" of bright, Stokes-shifted light.[40-43] Chemical enhancement involves shifting and broadening the electronic states of the absorbant through their interactions with the metal surfaces they are bound to.[42] Known as surface-enhanced Raman spectroscopy (SERS), this spectroscopic technique allows for single-particle analysis at room temperature by amplifying these "hot spots" to enhance the Stokes and anti-Stokes signals by 14 orders of magnitude.[40,41] This signal is still fairly weak, however, because a majority of the molecules in a targeted sample are not Raman-active.[40,41] SERS can be further amplified by exploiting this effect and resonance Raman enhancement effect, where the frequency of the exciting radiation coincides with or is in the region of an electronic absorption band in the targeted molecule.[39,40] Known as surface-enhanced resonance Raman spectroscopy (SERRS), this technique combines that of SERS as well as utilizing the absorption of an incident photon to promote an electron into an excited vibronic state and immediately relaxing to a vibrational level of the ground state, providing low detection limits suitable for trace analysis

without the need of chemical enhancement.[39,41] The analytical enhancement factor (AEF) of a SERRS substrate can then be calculated by comparing the signal of the SERRS sample to the non-enhanced Raman signal of the target analyte using the following Equation 1.1:

$$AEF = \frac{[I/(M \times t)]_{\text{SERRS}}}{[I/(M \times t)]_{\text{Raman}}} \quad (1.1)$$

where *I* is the intensity of the spectrum, *M* is the concentration of the analyte in solution, and *t* is the integration time in seconds.

SERS and SERRS have a variety of applications. In cell biology, Au NPs are used because of their favorable physical and chemical properties and biocompatibility.[41] For example, in SERS sensing, an *in vivo* glucose sensor can monitor glucose fluctuations throughout the day or a SERS sensor using AgFON can also be fabricated to quantitatively detect an anthrax biomarker.[43] However, the analyte of interest must be placed within nanometers of the metal surface in order to be detected, so the ability to control the size, shape and orientation of the NPs on a surface while minimizing aggregation is necessary to reduce many complex variables and greatly enhance the understanding of this phenomenon.[43]

## 1.6 Polymer Microgels

Polymer microgels have a multifunctionality in their chemical and physical properties that allow for thermo- and pH-responsivity. In the case where temperature sensitive groups are present in the polymer network, when the solution temperature is below a characteristic lower critical solution temperature (LCST), the micelles are highly swollen in water and after heating they shrink rapidly to become a collapsed polymer globule, allowing the fabrication of "switchable" or "stimuli-responsive" materials.[44-47] Likewise, when acid/base sensitive groups are present, if the

pH is cycled above and below the critical pH of the microgel, the globules will swell and shrink in a reversible process.[46,48-50] The swelling ability of a microgel depends on the type of microgel, affinity to the solvent, ionic strength, monomer composition/concentration, and degree of crosslinking.[44] Incorporating ionic monomers such as acrylic acid, vinylimidazole, and 4-vinylpyridine allows for these polymers to become pH-sensitive.[45] Some other classes of pH-responsive microgels also include: methacrylic acid-based alkali-swellable latexes; N-isopropylacrylamide-based copolymer microgels containing either acidic or basic comonomers; and acid-swellable latexes based on basic monomers such as 2-vinylpyridine or tertiary amine methacrylates.[48,50] A general example of such latex polymers can be seen in **Figure 1.4** and **1.5**.

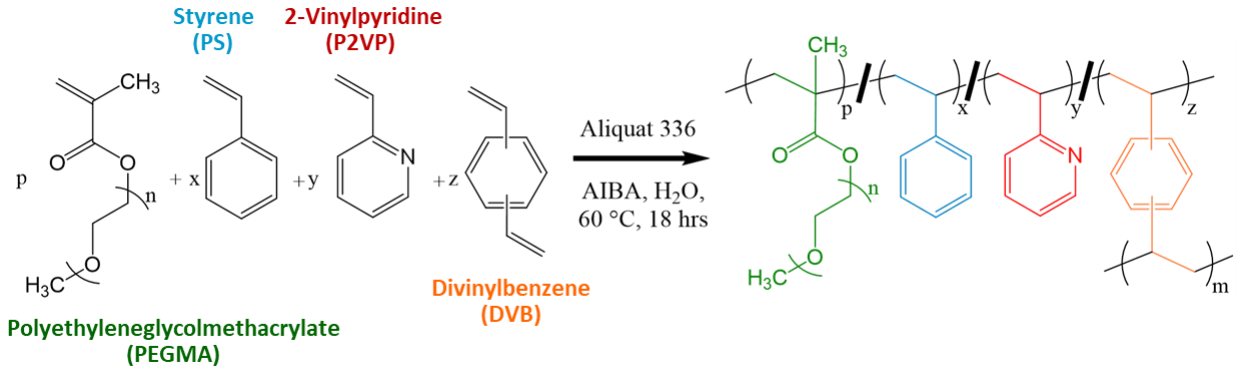


**Figure 1.4**. Generalized chemical equation for the synthesis of a sterically stabilized pH-responsive latex from a random copolymer of styrene and 2-vinylpyridine ($PS_xP2VP_y$).[51]

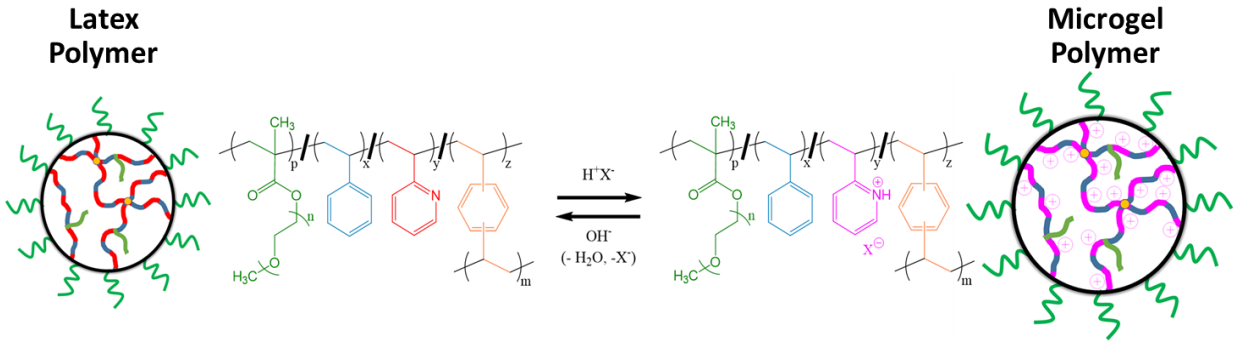


**Figure 1.5**. Generalized chemical equation for the reversible transition of sterically stabilized $PS_xP2VP_y$ latex into sterically stabilized $PS_xP2VP_y$ microgel upon addition of a Brønsted-Lowry acid.[51]

These microgels are so versatile that they have been used in a variety of applications. They have been used as containers for drug delivery, agents for targeting cancer cells, biosensors, particulate emulsifiers, detectors for poisonous substances in food or the environment, biological warfare sensors, and viscosity modifiers for cosmetics and pharmaceutical formulations.[44-50] If the carrier is able to disassemble when arriving at a target cancer cell because of the local pH, the release of the drug is facilitated; however, there is a limitation of circulation *in vivo* for therapeutic activity due to the poor solubility of the hydrophobic polymers.[49] Incorporating magnetic NPs into the polymeric particles, microgels, capsules or hydrogels has received interest due to the extraordinary properties of these composite materials in a magnetic field, which also can solve the problem of stabilization in physiological environments.[44,45,50] Bhattacharya *et. al.* discovered that loading up to 15 wt% of magnetite into the thermosensitive microgel shell allows for controlled drug release in a magnetic field, which makes these microgels interesting candidates for hyperthermia cancer treatment.[45] Likewise, quantum dots have found use in these microgels for controlled drug release via a temperature or pH-dependent reversible process.[50]

Polymeric materials recently have found use in SERS studies. High SERS activity is predominantly based on the plasmonic "hot spots" that can give rise to high enhancement factors, so it is desired to prepare a SERS-active substrate with large numbers of hot spots in order to sense targeted molecules with high efficiency.[46] Akamatsu *et. al.* discovered that by combining the unique size-dependent properties of metal NPs with the macroscopic size-controllable properties of polymer gels, it is possible to control the size, shape, and location of the NPs in or on the microgels in order to optimize the SERS-active "hot spots" on the particles; the size and interparticle distance of metal NPs determines the quantum size effects and particle-to-particle

interactions within a system.[50] The interparticle distance ($i_{pd}$) can be calculated using the following Equation 1.2:

$$i_{\mathrm{pd}} = \sqrt{\frac{A}{N}} - d_{\mathrm{NP}} \tag{1.2}$$

where *A* is the surface area of the polymer micelle, *N* is the number of NPs on the surface, and $d_{NP}$ is the average diameter of the NPs.

Curtis *et. al.* likewise reported that these interparticle "hot spots" on the polymeric particles can be tuned via pH adjustments, and this process is reversible over an extended period of time; increasing the pH of the system decreases the $i_{pd}$ distance between the metal NPs on the surface of the polymer beads, thereby increasing the SERS signals, and vice versa.[51] Therefore, it is desired to develop a SERS substrate that can be fine-tuned to optimize the signals obtained.

The following project describes the synthesis and analysis of a multifunctional particle system used as a SERS substrate, optimizing the system described by Curtis *et. al*. The size of the Au NPs on the surface of the polymer micelle beads are tuned through a further reduction of silver or gold ions to optimize signal output for bulk SERS and single-particle SERS with crystal violet as the reporting molecule. These signals are further optimized by altering the pH of the multifunctional particle system between acidic and basic conditions to prove stability and reversibility.

## 1.7 References

1. Fan, M.; Andrade, G. F. S.; Brolo, A. G. A review on the fabrication of substrates for surface enhanced Raman spectroscopy and their applications in analytical chemistry. *Anal. Chem. Acta.*, **2011**, *623*, 7-25.
2. Zhu, H.; Fan, J.; Wang, B.; Peng, X. Fluorescent, MRI, and colorimetric chemical sensors for the first-row d-block metal cations. *Chem. Soc. Rev.*, **2015**, *44*, 4337-4366.

3. Jiang, Z.; Le, N. D. B.; Gupta, A.; Rotello, V. M. Cell surface-based sensing with metallic nanoparticles. *Chem. Soc. Rev.*, **2015**, *44*, 4264-4274.
4. Silvi, S. and Credi, A. Luminescent sensors based on quantum dot–molecule conjugates. *Chem. Soc. Rev.*, **2015**, *44*, 4275-4289.
5. Bunz, U. H. F.; Seehafer, K.; Bender, M.; Porz, M. Poly(aryleneethynylene)s (PAE) as paradigmatic sensor cores. *Chem. Soc. Rev.*, **2015**, *44*, 4322-4336.
6. Yang, J.-S. and Swager, T. M. Fluorescent porous polymer films as TNT chemosensors: electronic and structural effects. *J. Am. Chem. Soc.*, **1998**, *120*, 11864.
7. He, G.; Yan, N.; Yang, J.; Wang, H.; Ding, L.; Yin, S.; Fang, Y. Pyrene-containing conjugated polymer-based fluorescent films for highly sensitive and selective sensing of TNT in aqueous medium. *Macromolecules*, **2011**, *44*, 4759.
8. Singha, S.; Kim, D.; Seo, H.; Cho, S. W.; Ahn, K. H. Fluorescence sensing systems for gold and silver species. *Chem. Soc. Rev.*, **2015**, *44*, 4367-4399.
9. Chatterjee, A.; Santra, M.; Won, N.; Kim, S.; Kim, J. K.; Kim, S. B.; Ahn, K. H. Selective fluorogenic and chromogenic probe for detection of silver ions and silver nanoparticles in aqueous media. *J. Am. Chem. Soc.*, **2009**, *131*, 2040.
10. Tong, H.; Wang, L.; Jing, X.; Wang, F. Highly selective fluorescent chemosensor for silver (I) ion based on amplified fluorescence quenching of conjugated polyquinoline. *Macromolecules*, **2002**, *35*, 7169.
11. Lin, C.-Y.; Yu, C.-J.; Lin, Y.-H.; Tseng, W.-L. Colorimetric sensing of silver (I) and mercury (II) ions based on an assembly of tween 20-stabilized gold nanoparticles. *Anal. Chem.*, **2010**, *82*, 6830.
12. Huy, G. D.; Zhang, M.; Zuo, P.; Ye, B.-C. Multiplexed analysis of silver (I) and mercury (II) ions using oglionucletide-metal nanoparticle conjugates. *Analyst*, **2011**, *136*, 3289.
13. Meyer, R.; Lemire, C.; Shaikhytdinov, S. K.; Freund, H.-J. Surface chemistry of catalysis by gold. *Gold Bull.*, **2004**, *37*, 72.
14. Wilson, R. The use of gold nanoparticles in diagnostics and detection. *Chem. Soc. Rev.*, **2008**, *37*, 2028.
15. Best, S. L. and Sadler, P. J. Gold drugs: mechanism of action and toxicity. *Gold Bull.*, **1996**, *29*, 87.
16. Parish, R. V. and Cottrill, S. M. Medicinal gold compounds. *Gold Bull.*, **1987**, *20*, 3.
17. Krikavova, R.; Hosek, J.; Vanco, J.; Hutyra, J.; Dvorak, Z.; Travnicek, Z. Gold (I)-triphenylphosphine complexes with hypoxanthine-derived ligands: In vitro evaluations of anticancer and anti-inflammatory activities. *PLoS One*, **2014**, *9*, e107373.
18. Milacic, V.; Fregona, D.; Dou, Q. P. Targeting the ubiquitin-proteasome pathway with inorganic compounds to fight cancer: a challenge for the future. *Histol. Histopathol.*, **2008**, *23*, 101.
19. Bajaj, A.; Miranda, O. R.; Kim, I.-B; Phillips, R. L.; Jerry, D. J., Bunz, U. H. F.; Rotello, V. M. Detection and differentiation of normal, cancerous, and metastatic cells using nanoparticle-polymer sensor arrays. *Proc. Natl. Acad. Sci. U. S. A.*, **2009**, *106*, 10912–10916.
20. Sha, M. Y.; Zu, H.; Natan, M. J.; Cromer, R. Surface-enhanced Raman scattering tags for rapid and homogeneous detection of circulating tumor cells in the presence of human whole blood. *J. Am. Chem. Soc.*, **2008**, *130*, 17214-17215.
21. Qian, X.; Peng, X.-H.; Ansari, D. O.; Yin-Goen, Q.; Chen, G. Z.; Shin, D. M.; Yang, L.; Young, A. N.; Wang, M. D.; Nie, S. *In vivo* tumor targeting and spectroscopic detection with surface-enhanced Raman nanoparticle tags. *Nat. Biotechnol.*, **2008**, *26*, 83-90.

22. Jelinek, R. and Kolusheva, S. Carbohydrate biosensors. *Chem. Rev.*, **2004**, *104*, 5987-6016.
23. Daraee, H.; Eatemadi, A.; Abbasi, E.; Aval, S. F.; Kouhi, M.; Akbarzadeh, A. Application of gold nanoparticles in biomedical and drug delivery. *Artifical Cells, Nanomed., and Biotechnol.* **2014**, *44*, 410-422.
24. Abbasi, E.; Milani, M.; Aval, S. F.; Kouhi, M.; Akbarzadeh, A.; Nasrabadi, H. T.; Nikasa, P.; Joo, S. W.; Hanifehpour, Y.; Nejati-Koshki, K.; Samiei, M. Silver nanoparticles: Synthesis methods, bio-applications and properties. *Crit. Rev. in Microbio.* **2014**, *42* (2), 173-180.
25. Li, L-S.; Hu, J.; Yang, W.; Alivisatos, A. P. Band gap variation of size- and shape-controlled colloidal CdSe quantum rods. *Nano Lett.* **2001**, *1*, 349-351.
26. Chiu, Y. L. and Rana, T. M. siRNA function in RNAi: a chemical modification analysis. *RNA.* **2003**, *9*, 1034-1048.
27. Dhar, S.; Daniel, W. L.; Giljohann, D. A.; Mirkin, C. A.; Lippard, S. J. Polyvalent oligonucleotide gold nanoparticle conjugates as delivery vehicles for platinum (IV) warheads. *J. Am. Chem. Soc.* **2009**, *131*, 14652-14653.
28. Jeynes, J. C.; Jeynes, C.; Merchant, M. J.; Kirkby, K. J. Measuring and modelling cell-to-cell variation in uptake of gold nanoparticles. *Analyst.* **2013**, *138*, 7070-7074.
29. Faraday, M. Experimental Relations of Gold (and Other Metals) to Light. *Philos. Trans.* **1857**, *147*, 145-181.
30. Mulfinger, L.; Solomon, S. D.; Bahadory, M.; Jeyarajasingam, A. V.; Rutkowsky, S. A.; Boritz, C. Synthesis and Study of Silver Nanoparticles. *J. Chem. Educ.* **2007**, *84*, 322.
31. Lee, P. C. and Meisel, D. Adsorption and surface-enhanced Raman of dyes on silver and gold sols. *J. Phys. Chem.* **1982**, *86*, 3391-3395.
32. Akamatsu, K.; Shimada, M.; Tsuruoka, T.; Nawafune, H.; Fujii, S.; Nakamura, Y. Syntehsis of pH-Responsive Nanocomposite Microgels with Size-Controlled Gold Nanoparticles from Ion-Doped, Lightly Cross-Linked Poly(vinylpyridine). *Langmuir* **2010**, *26*, 1254-1259.
33. Frens, G. Contrlled Nucleation for the Regulation of the Particle Size in Monodisperse Gold Suspensions. *Nature, Phys. Sci.* **1973**, *241* (105), 20-22.
34. Evanoff, D. D. and Chumanov, G. Size-controlled synthesis of nanoparticles: measurement of extinction, scattering, and absorption cross sections. *J. Phys. Chem. B.* **2004**, *108*, 13957-13962.
35. Wiley, B.; Sun, Y.; Mayers, B.; Xia, Y. Shape controlled synthesis of metal nanostructures: the case of silver. *Chem. A. Eur. J.* **2005**, *11*, 454-463.
36. Jana, N. R.; Gearheart, L.; Murphy, C. J. Evidence for Seed-Mediated Nucleation in the Chemical Reduction of Gold Salts to Gold Nanoparticles. *Chem. Mater.* **2001**, *13*, 2313-2322.
37. Stamatoiu, O.; Mirzaei, J.; Feng, X.; Hegmann, T. Nanoparticles in liquid crystals and liquid crystalline nanoparticles in liquid crystals. *Springer*. **2012**, 331-393.
38. Abadeer, N. S. and Murphy, C. J. Recent Progress in Cancer Thermal Therapy Using Gold Nanoparticles. *J. of Phys. Chem. C.* **2016**, *120* (9), 4691-4716.
39. Ingle, Jr., J. D.; Crouch, S. R. "Molecular Scattering Methods." *Spectrochemical Analysis*; Prentiss Hall: Englewood Cliffs, **1998**, 494-513.
40. Nie, S.; Emory, S. R. Probing Single Molecules and Single Nanoparticles by Surface-Enhanced Raman Scattering. *Science*. **1997**, *275*, 1102-1106.

41. Kniepp, K. & H. & J. Surface-Enhanced Raman Scattering in Local Optical Fields of Silver and Gold Nanoaggregates – From Single-Molecule Raman Spectroscopy to Ultrasensitive Probing in Live Cells. *Acc. Chem. Res.* **2006**, *39*, 443-450.
42. Campion, A.; Patanjali, K. Surface-enhanced Raman scattering. *Chem. Soc. Rev.* **1998**, *27*, 241-250.
43. Stiles, P. L.; Dieringer, J. A.; Shah, N. C.; Van Duyne, R. P. Surface-Enhanced Raman Spectroscopy. *Annu. Rev. Anal. Chem.* **2008**, *1*, 601-626.
44. Pich, A.; Bhattacharya, S.; Lu, Y.; Boyko, V.; Adler, H. J. P. Temperature-Sensitive Hybrid Microgels with Magnetic Properties. *Am. Chem. Soc.* **2004**, *20*, 10706-10711.
45. Bhattacharya, S.; Exkert, F.; Boyko, V.; Pich, A. Temperature-, pH-, and Magnetic-Field-Sensitive Hybrid Microgels. *Small*. **2007**, *3*, 650-657.
46. Chen, H.; You, T.; Jiang, L.; Gao, Y.; Yin, P. Creating dynamic SERS hotspots on the surface of pH-responsive microgels for direct detection of crystal violet in solution. *RSC Adv.* **2017**, *7*, 32743-32748.
47. Lu, Y.; Liu, G. L.; Lee, L. P. High-Density Silver Nanoparticle Film with Temperature-Controllable Interparticle Spacing for a Tunable Surface Enhanced Raman Scattering Substrate. *Nano Lett*. **2005**, *5*, 5-9.
48. Dupin, D.; Fujii, S.; Armes, S. P.; Reeve, P.; Baxter, S. M. Efficient synthesis of sterically stabilized pH-responsive microgels of controllable particle diameter by emulsion polymerization. *Langmuir*. **2006**, *22*, 3381-3387.
49. Martin, T. J.; Procházka, K.; Munk, P.; Webber, S. E. pH-Dependent Micellization of Poly(2-vinylpyridine)-block-poly(ethylene oxide). *Macromolecules*. **1996**, *29*, 6071-6073.
50. Akamatsu, K.; Shimada, M.; Tsuruoka, T.; Nawafune, H.; Fujii, S.; Nakamura, Y. Synthesis of pH-Responsive Nanocomposite Microgels with Size-Controlled Gold Nanoparticles from Ion-Doped, Lightly Cross-Linked Poly(vinylpyridine). *Langmuir*. **2010**, *26*, 1254-1259.
51. Curtis, T.; Taylor, A. K.; Alden, S. E.; Swanson, C.; Lo, J.; Knight, L.; Silva, A.; Gates, B. D.; Emory, S. R.; Rider, D. A. Synthesis and Characterization of Tunable, pH-Responsive Nanoparticle–Microgel Composites for Surface-Enhanced Raman Scattering Detection. *ACS Omega*. **2018**, *3*, 10572-10588.

# Chapter 2: Experimental Methods

The following chapter describes the experimental materials and methods used to develop multifunctional microgels usable for SERS substrates and imaging under a single-particle microscope. These particles consist polymer microgel beads made from a random copolymerization of polystyrene (PS) and 2-vinylpyridine (P2VP) at a ratio of 20:80. Au NPs are reduced on the surface of this $PS_{20}P2VP_{80}$ system *in vitro* to formulate a SERS active substrate that is tunable via pH adjustments. Silver or gold ions are further reduced onto the Au NP surface of these AuNP-$PS_{20}P2VP_{80}$ system to further enhance the SERS signal.

The synthesis methods used for the formulation and characterization of Ag@AuNP-$PS_{20}P2VP_{80}$ and Au@AuNP-$PS_{20}P2VP_{80}$ are described. Also described are the SERS spectroscopic methods used to optimize and analyze the Raman peaks in response to pH using both bulk SERS and single-particle SERS instrumentation.

## 2.1 Synthesis Materials and Methods

### 2.1.1 $PS_{20}P2VP_{80}$ Microgel Synthesis

*Materials.* The following reagents were used: styrene (PS, 99%, stabilized; Acros), 2-vinylpyridine (2VP, 97%, stabilized; Acros), divinylbenzene (DVB, 55%; Aldrich), N-methyl-N,N,N-trioctyloctan-1-ammonium chloride (Aliquat 336; Alfa Aesar), Poly(ethylene glycol) methyl ether methacrylate solution (PEGMA; Aldrich), 2,2'-Azobis(2-methylpropionamide) dihydrochloride (AIBA, 98%; Acros), and Ultrapure water was used for all aqueous solutions (17.5 MΩ-cm; Barnstead NANOpure purification system).

*Methods*. The method described is a modified procedure outlined by Dupin *et. al*.[1] The PS, 2VP and DVB were purified with columns containing glass wool and alumina sand to remove the

inhibitor molecules contained in the stock solutions. Excess purified monomer was stored in covered vials in the dark at -18 °C for up to three days. The emulsion polymerization was carried out in a 100 mL single-necked round-bottom reaction flask with stopcock attached to a vacuum-nitrogen hood Schleck line. The PEGMA stabilizer (0.420 mL) and Aliquat 336 surfactant (0.15 g) were dissolved in ultrapure water (40.00 mL) in the reaction flask and sealed with a rubber septum. The reaction flask contents were deaerated with 30 min of nitrogen bubbling, and the flask was placed in a hot oil bath set at 70 °C. The contents stirred at 500 rpm until stabilization. A scintillation vial was purged with nitrogen gas until deaerated. 2VP (4.00 g), PS (1.00 g) and DVB (0.03 g) were mixed into the inert scintillation vial for a total targeted amount of 5.03 g. The contents of the monomer vial were transferred to the reaction flask using a syringe equipped with a filter (PTFE, 0.45 μm, Millex). An emulsified condition was established by continual stirring (500 rpm, 70 °C) for approximately 10 min. Deaerated, ultrapure water (5.00 mL) was used to pre-dissolve the AIBA initiator (0.050 g) in a separate scintillation vial. Once dissolved, the AIBA solution was rapidly delivered to the reaction flask via a syringe to initiate the polymerization reaction. Stirring continued for 21 h. Purification of the resulting latex was achieved by centrifuging the crude latex for 15 min at 10,000 rpm in high-density polycarbonate tubes (Thermo Scientific). After decanting the supernatant liquid, an addition of ultrapure water was made to bring the volume of the latex solution back to its original level. Redispersion was carried out by stirring via a Vortex mixer until the solution appeared uniform. Purification was repeated for a total of three cycles. The final latex solution was stored at 4 °C (9 wt%; ~80% yield).

### 2.1.2 AuNP-$PS_{20}P2VP_{80}$ Synthesis

*Materials.* The reagents listed in **$PS_{20}P2VP_{80}$ Microgel Synthesis** along with the following were used: potassium gold (III) perchlorate (99%, Acros), dimethylamine borane (DMAB, Sigma Aldrich), and Ultrapure water for all aqueous solutions (17.5 MΩ-cm; Barnstead NANOpure purification system). Dialysis tubing (Fisherbrand, 28.6 mm diameter, 20 μm thickness, Nominal MWCO 12,000-14,000) was used for all dialysis purification steps.

*Methods.* The method described is a modified procedure outlined by Chen *et. al.*[2] The method follows the same procedure as **$PS_{20}P2VP_{80}$ Microgel Synthesis** but with the following addition: an aliquat of 1.00 mL of the resulting polymer solution was diluted in 5.00 mL of Ultrapure water and mixed with 17.50 mL of 20 mM $KAuCl_4$ for one hour. The resulting solution was purified via dialysis for 48 hours. Then 5.00 mL of 10 mM DMAB was added to 1.00 mL of the resulting ion-doped microgels at a rate of 150 μL per second. The solution stirred for one hour and was purified via dialysis for 24 h. For both dialysis steps, Ultrapure water was used and the baths were changed every 8 h.

### 2.1.3 Ag@AuNP-$PS_{20}P2VP_{80}$ Synthesis

*Materials.* The reagents listen in **AuNP-$PS_{20}P2VP_{80}$ Synthesis** along with the following were used: sodium citrate (dihydrate, Mallinckrodt Chemicals), silver (I) nitrate (Mallinckrodt Chemicals), ascorbic acid (Baker Chemicals), ammonium hydroxide (99.99%, Fisher), and Ultrapure water for all aqueous solutions (17.5 MΩ-cm; Barnstead NANOpure purification system).

*Methods.* The method described is a modified procedure outlined by Fales *et. al.*[3] The method follows the same procedure as **AuNP-$PS_{20}P2VP_{80}$ Synthesis** but with the following

addition: an aliquat of 1.00 mL of the resulting AuNP-Polymer solution was diluted in 5.00 mL of Ultrapure water and mixed with 1.00 mL of 38.8 mM sodium citrate. The solution stirred for one hour to stabilize. Then 50 µL of 0.1 M $AgNO_3$ and 50 µL of 0.1 M ascorbic acid were added to the solution, and the solution was spiked with 10 µL of concentrated ammonium hydroxide to rapidly increase the pH of the system. The solution stirred for 30 min. and was purified by centrifugation at 5,000 RPM for 15 min.

### 2.1.4 Au@AuNP-$PS_{20}P2VP_{80}$ Synthesis

*Materials*. The reagents listed in **AuNP-$PS_{20}P2VP_{80}$ Synthesis** along with the following were used: sodium citrate (dihydrate, Mallinckrodt Chemicals), hydroxylamine hydrochloride (J.T. Baker), and Ultrapure water for all aqueous solutions (17.5 MΩ-cm; Barnstead NANOpure purification system).

*Methods.* The method described is a modified procedure outlined by Jenkins *et. al.*[4] The method follows the same procedure as **AuNP-$PS_{20}P2VP_{80}$ Synthesis** but with the following addition: an aliquat of 1.00 mL of the resulting AuNP-Polymer solution was diluted in 13.00 mL of Ultrapure water and mixed with 250 µL of 38.8 mM sodium citrate. The solution stirred for 4 min. before 25 mM $KAuCl_4$ was added dropwise to the solution. The solution stirred for 8 min. before 10 mM hydroxylamine hydrochloride was added at a rate of 10 drops per second. The reagent volume ratios for each growth synthesis are outlined in **Table 2.1**. The solution stirred for one hour and the resulting particles were purified via centrifugation at 5,000 RPM for 15 min.

**Table 2.1.** Chemicals for seed-mediated NP growth. Different size Au NPs are prepared by using the prescribed volumes.

| Solution | AuNP-$PS_{20}P2VP_{80}$ (mL) | $H_2O$ (mL) | $Na_3C_6H_5O_7$ (µL) | $KAuCl_4$ (µL) | $NH_2OH{\cdot}HCl$ (µL) |
|---|---|---|---|---|---|
| **1** | 1.00 | 13.00 | 250 | 57.5 | 85.0 |
| **2** | 1.00 | 13.00 | 250 | 230 | 340 |

## 2.2 Characterization of Multifunctional Microgels

*STEM.* Scanning transmission electron microscopy (STEM) data was collected on a JEOL Field Emission scanning electron microscope (JEOL SM-13020RLV). Samples were prepared by applying a 2-3 µL aliquat directly to a carbon 300 mesh copper TEM grid (Formvar) to dry and imaged with a STEM detector.

*EDS.* Energy-dispersive x-ray spectroscopy (EDS) data was collected on a JEOL Field Emission scanning electron microscope (JEOL SM-13020RLV). Samples were prepared by applying a 2-3 µL aliquat directly to a carbon 300 mesh copper TEM grid (Formvar) to dry and analyzed with an EDS detector.

*AFM.* Atomic force microscopy (AFM) data was collected on a low-power microscope stage (TS-300/LT) with a Nikon Eclipse T*i*-U camera attachment. Samples were prepared by applying a 10 µL aliquat directly to a coverslip slide to dry. The coverslip slide was taped to a microscope slide prior to placing in the instrument. The tapping-mode scan rate was set to 1.00 Hz with 512 samples per line and the ScanAsyst Auto Control settings turned on.

*UV-Vis.* Ultraviolet-visible (UV-Vis) extinction spectra were acquired with a diode array UV-Vis spectrophotometer (Jasco V-670; WWU 380) using 10.00 mm polystyrene cells (Fisher).

The AuNP-$PS_{20}P2VP_{80}$ particles were diluted by a factor of 10 prior to acquiring spectra; all other solutions were analyzed at the original concentration.

## 2.3 SERS Instrumentation

### 2.3.1 Bulk SERRS

Bulk SERS instrumentation was used to analyze crystal violet (CV) as a reporter molecule for surface-enhanced resonance Raman scattering (SERRS) spectroscopy. To prepare a bulk SERRS sample, 890 µL of the sample was mixed with 10 µL of $10^{-6}$ M CV solution. Then 450 µL of the resulting solution was measured into a collection tube and analyzed on a bulk Raman instrument with a 633 nm wavelength HeNe laser (DeltaNu Advantage 200A) shown in **Figure 2.1** and **2.2**. The integration time for the spectra was 60 s and repeated for a total of five spectra.


**Figure 2.1**. Digital image of a bulk Raman Spectrometer with a 633 nm wavelength light source.

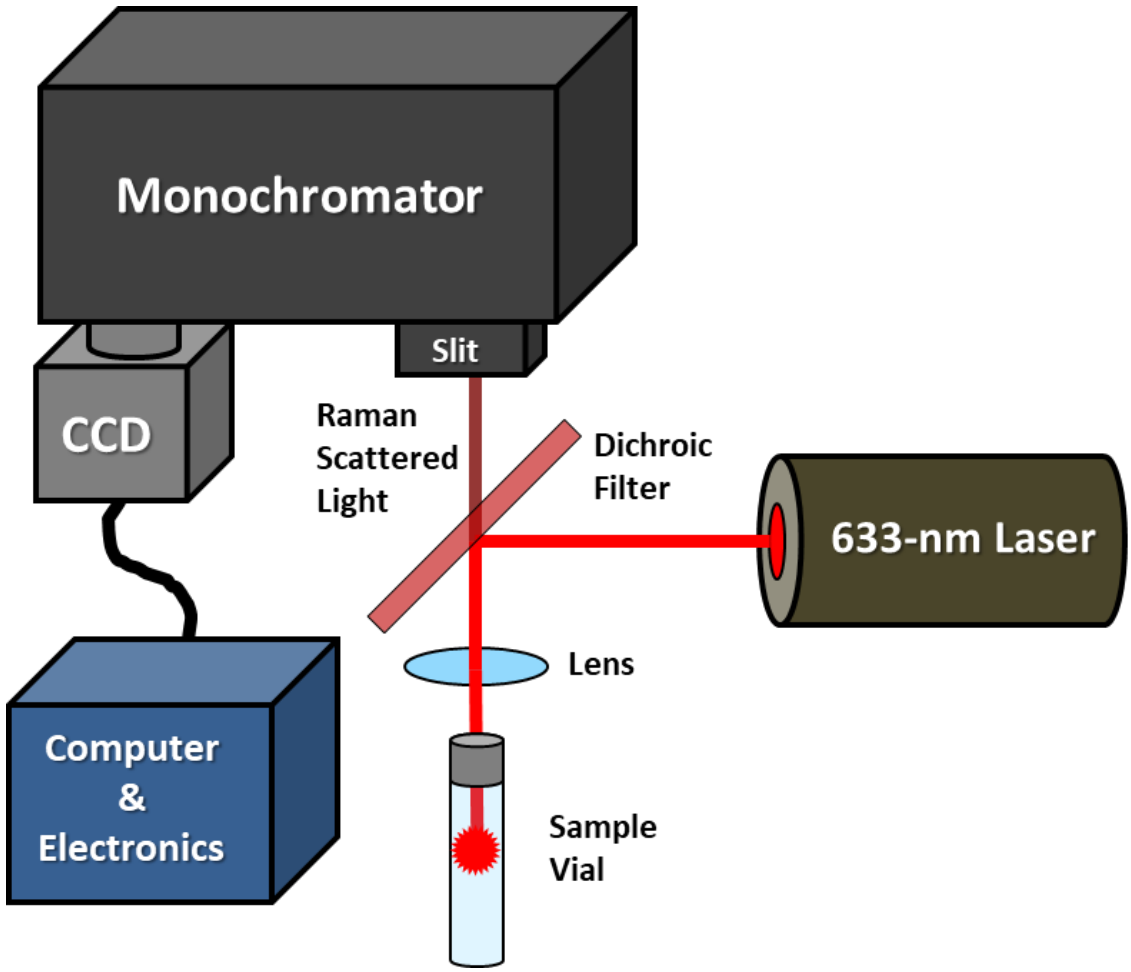


**Figure 2.2**. Schematic diagram of a bulk Raman laser system. The Raman scattered light passes through a dichroic filter into a monochromator coupled with a charged coupled device (CCD), where the data is then sent to a computer for processing.

### 2.3.2 Single-Particle SERRS

Single-particle SERS instrumentation was used to analyze CV as a reporter molecule for SERRS spectroscopy. To prepare a sample for single-particle SERRS, 890 µL of the sample was mixed with 10 µL of $10^{-5}$ M CV solution. Then 10 µL of the resulting solution was placed on a coverslip slide to dry and analyzed on a single-particle Raman microscope, with a 633 nm wavelength HeNe laser (linearly polarized; Melles Griot) filtered with an automated filter wheel and neutral density filters (Melles Griot) to a power of ~9 µW, and an inverted confocal microscope (Olympus IMT-2) mounted with a 100× 1.3 numerical aperture objective (Olympus) shown in **Figure 2.3** and **2.4**. The motorized stage was controlled manually. The laser passed through a band-pass filter (ThorLabs) and was focused through an entrance slit opened to 2 mm to optimize throughput of a single-stage spectrograph (Triax 320; Jobin Yvon; 1200 g/mm; 500 nm blaze). Spectra were acquired with an electrothermally cooled charge-coupled device (CCD) camera (Andor 100 × 1024 pixels; DV401-BV) controlled by both Andor MCD and LabView 8.0 software (National Instruments). The spectra were acquired via a kinetic series on a single-track readout mode of 16 µs per pixel with an integration time of 5 s per spectra and repeated for a total of 20 spectra.

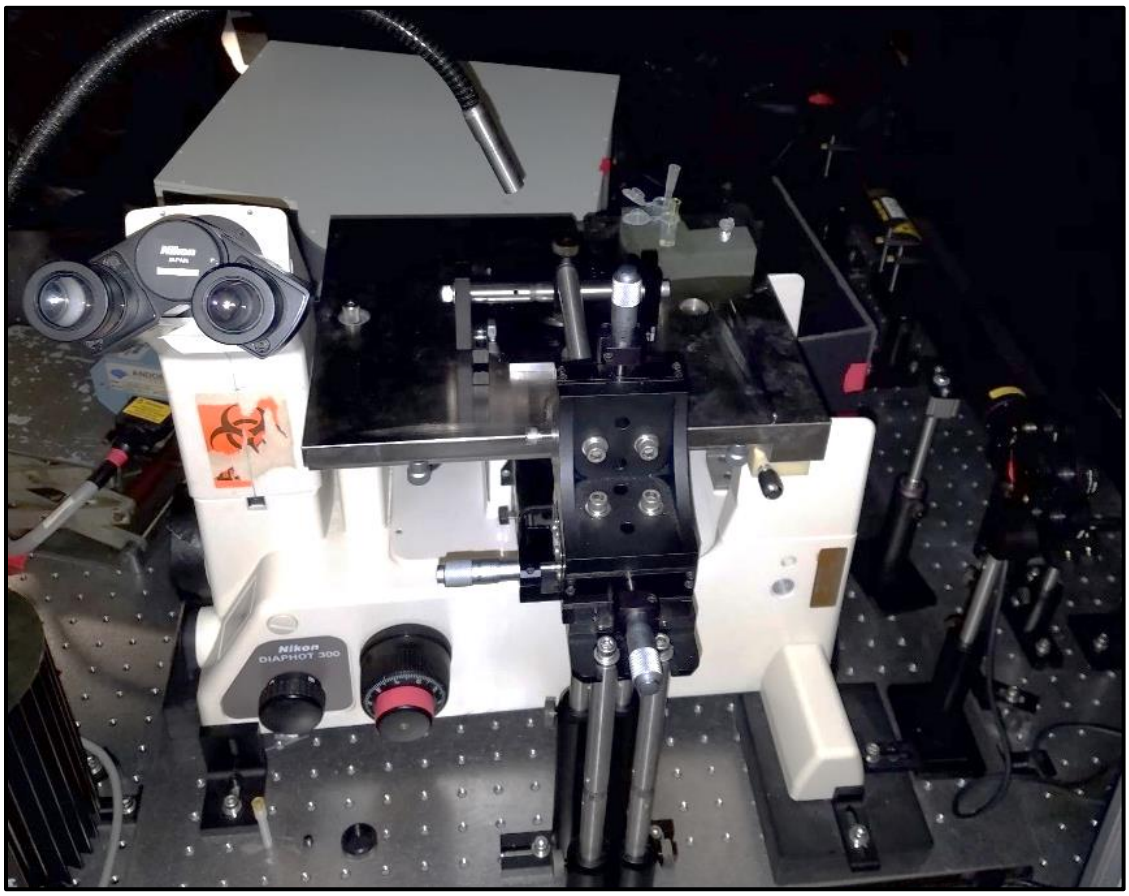


**Figure 2.3**. Digital image of a single-particle Raman Spectrometer with a 633 nm wavelength light source and a microscope stage mount.

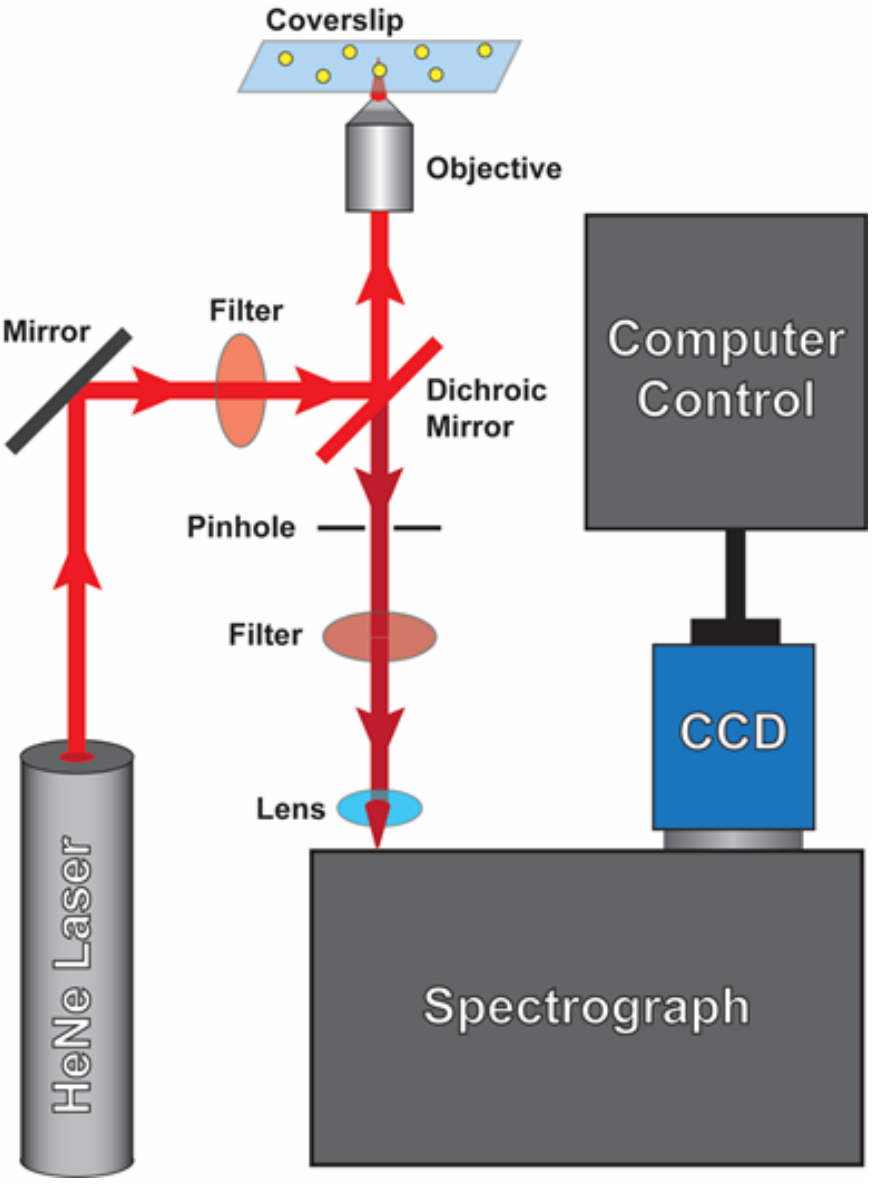


**Figure 2.4**. Schematic diagram of a single-particle Raman laser system. The HeNe laser passes through a filter and reflects off a dichroic mirror and is focused onto a single particle on a surface. The Raman scattered light passes through the dichroic mirror into a monochromator coupled with a charged coupled device (CCD), where the data is then sent to a computer for processing.

## 2.4 pH Cycling of Multifunctional Microgels

*Materials.* The following reagents were used for all pH adjustments: hydrochloric acid (38.0%, Sigma Aldrich), sodium hydroxide (97%, Sigma Aldrich), and Ultrapure water for all aqueous solutions (17.5 MΩ-cm; Barnstead NANOpure purification system).

*Bulk SERRS.* The parameters described in **Bulk SERRS** were used with the following adjustments: the sample in the collection tube was spiked with 10 µL of 0.10 M HCl to adjust the sample to a low pH (from pH ≈ 6 to pH ≈ 4). The sample was mixed thoroughly and the spectra were obtained. The sample was then spiked with 10 µL of 0.10 M NaOH to increase the pH back to the starting value. The sample was mixed thoroughly and the spectra were obtained. This pH cycling continued for five full pH cycles. The integration time for the spectra at each condition was 60 s and repeated for three spectra per pH adjustment.

*Single-Particle SERRS.* The parameters described in **Single-Particle SERRS** were used with the following adjustments: the sample on the coverslip slide was spiked with 10 µL of 2.2 mM HCl to adjust the sample to a low pH (from pH ≈ 6 to pH ≈ 4), and the spectra were obtained. A pipette was used to remove the HCl from the coverslip slide, leaving the dried particles remaining on the coverslip slide. The sample was spiked with 10 µL of 2.2 mM NaOH to increase the pH back to the starting value. After 10 min the NaOH was pipetted off the slide, and the slide was spiked with another 10 µL of 2.2 mM NaOH to adjust the sample to a high pH (from pH ≈ 6 to pH ≈ 8) before the spectra were obtained. This extra spike of NaOH was to ensure that the pyridine group of the polymer micelles was fully deprotonated prior to obtaining spectra. This pH cycling continued for five full pH cycles, and repeated for three differing particles. The spectra were acquired via a kinetic series on a single-track readout mode of 16 µs per pixel with an integration time of 5 s per spectra and repeated for 10 spectra per pH adjustment.

## 2.5 References

1. Dupin, D.; Fujii, S.; Armes, S. P.; Reeve, P.; Baxter, S. M. Efficient synthesis of sterically stabilized pH-responsive microgels of controllable particle diameter by emulsion polymerization. *Langmuir* **2006**, *22*, 3381-3387.
2. Chen, H.; You, T.; Jiang, L.; Gao, Y.; Yin, P. Creating dynamic SERS hotspots on the surface of pH-responsive microgels for direct detection of crystal violet in solution. *RSC Adv.* **2017**, *7*, 32743-32748.
3. Fales, A. M.; Yuan, H.; Vo-Dinh, T. Development of Hybrid Silver-Coated Gold Nanostars for Nonaggregated Surface-Enhanced Raman Scattering. *J. of Phys. Chem. C*, **2014**, *118*, 3708-3715.
4. Jenkins, J. A.; Wax, T. J.; Zhao, J. Seed-Mediated Synthesis of Gold Nanoparticles of Controlled Sizes to Demonstrate the Impact of Size on Optical Properties. *J. of Chem. Ed.* **2017**, *94*, 1090-1093.

# Chapter 3: Results and Discussion

Results are reported on the development of multifunctional microgels for the use of surface-enhanced resonance Raman scattering (SERRS) properties of Au NPs on the surface of these microgels. The synthesis methods for all components of these SERRS substrates are discussed, along with the SERRS method used in testing the microgel response to changes in chemical environments. Results are discussed for both bulk SERS and single-particle SERS instrumentation to compare the sensitivities of both methods through their optimized SERRS parameters. Lastly, presented are descriptions of possible future functionality inclusions to these multifunctional particles to further optimize SERRS parameters.

## 3.1 Multifunctional Microgel Synthesis

*SERS Substrate Overview.* For biological applications, and ideal SERS substrate uses near-infrared (NIR) excitation to minimize fluorescence and maximize tissue penetration. Metal NPs smaller than 100 nm possess a size-tunable excitation into the red to NIR region of the electromagnetic spectrum (600 – 1200 nm) and produce consistent SERS spectral results. Ideally, the substrate needs to decrease the distance between the metal NPs in order to prevent aggregation, which limits reproducibility. Binding metal NPs to the surface of polymer microgels and adjusting the pH of the system through a reversible process can control the interparticle distance and thus control the SERS enhancement.

The SERS signal optimization can be achieved by fine-tuning not only the pH of the polymeric system, but also the size, shape, and concentration of the metal NPs on the surface of the polymer microgels. The reduction of silver or gold ions onto Au NPs adsorbed to polymer microgels consisting of 20% polystyrene and 80% 2-vinylpyridine (Ag@Au-$PS_{20}P2VP_{80}$ or

Au@Au-$PS_{20}P2VP_{80}$) was explored as SERS substrates for both bulk SERS and single-particle SERS applications. The Au NPs are more biocompatible with a surface plasmon resonance (SPR) peak of individual particles above 500 nm and allow for the excitation through a 633 nm laser. Reducing silver or gold ions to the surface of the AuNP-$PS_{20}P2VP_{80}$ allows for the tuning of the NP size to further optimize the SERS signal by matching the NPs SPR.

### 3.1.1 $PS_{20}P2VP_{80}$ Microgels

The polymer microgels with an average homogeneous size distribution of ~275 nm in diameter were successfully synthesized via an emulsion polymerization reaction method. A SEM micrograph image is presented in **Figure 3.1**. The concentration of the $PS_{20}P2VP_{80}$ solution is calculated at ~$10^{12}$ particles/mL.

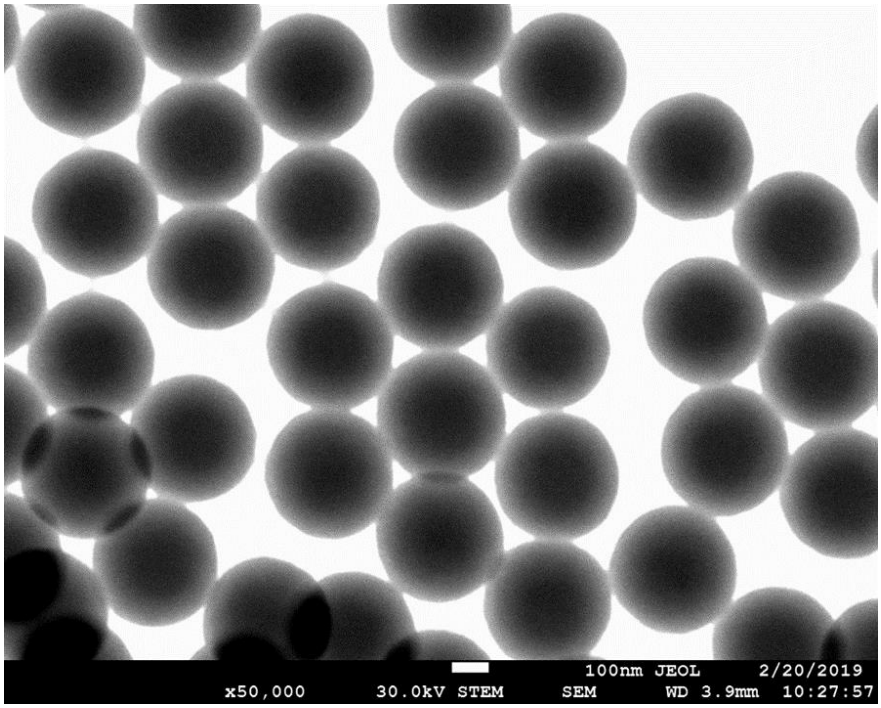


**Figure 3.1**. STEM image of monodisperse $PS_{20}P2VP_{80}$ microgels. The scale bar is 100 nm.

In a previous study completed by Curtis *et. al*, the polymer swelling size distribution was found to be dependent not only on the pH of the solution, but also the percentage ratios between poly styrene (PS) and poly 2-vinylpyridine (P2VP). **Figure 3.2** shows that by increasing the percentage of P2VP in the microgel, the swelling diameter also increases under acidic conditions. Further studies showed that the 20% PS and 80% P2VP random co-polymer ($PS_{20}P2VP_{80}$) was the desirable ratio for pH cycling experiments; hydrating the pyridine group allowed for polymer solvation while the styrene group allowed for the diameter of the micelle to contract back to the original hydrodynamic diameter over several pH cycles.[1] Further studies demonstrated that increasing the ionic strength of the random co-polymer further stabilized the swelling and contracting ratios of the network as it alternated between latex and microgel state.[1] Using this information, it was decided to focus on developing a NP-polymer system using $PS_{20}P2VP_{80}$.

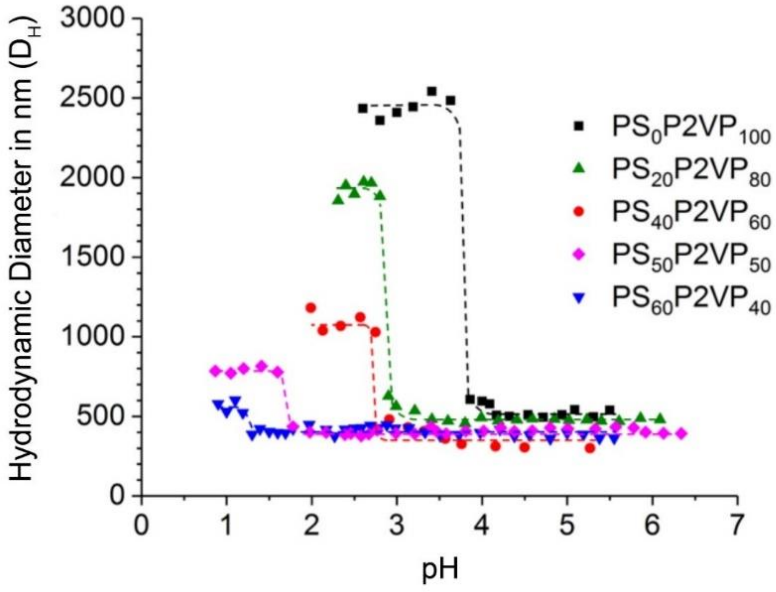


**Figure 3.2**. Reversible swelling and contracting of sterically stabilized $PS_xP2VP_y$ from microgel to latex form with increasing pH.[1]

**Figure 3.3** shows the size difference between dehydrated (latex) and hydrated (microgel) $PS_{20}P2VP_{80}$. The latex form of this polymer (pH ≈ 8) shows an average size distribution of ~275 nm in diameter while the microgel form (pH ≈ 4) shows an average size distribution of ~720 nm in diameter. In comparison to the data presented by Curtis *et. al*, the microgel presented a 4-fold

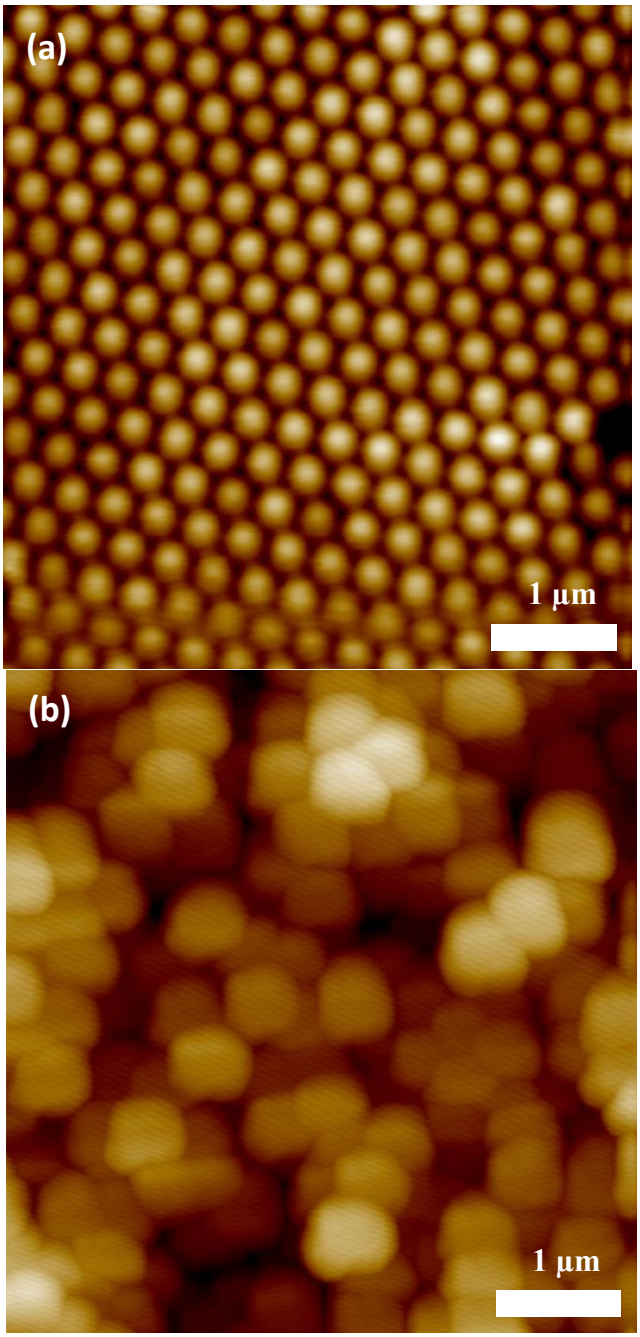


**Figure 3.3**. (a) AFM image of dehydrated $PS_{20}P2VP_{80}$ latex at pH ≈ 8. (b) AFM image of hydrated $PS_{20}P2VP_{80}$ microgels at pH ≈ 4.The scale bars are 1 µm.

increase in diameter in the DLS data and a 3-fold increase in the AFM data. This is likely due to the drying process of the sample used in the tapping-mode settings of the AFM. Although the sample was kept in a humid environment prior to analysis, some evaporation of the moisture of the sample was unavoidable, which would cause a slight contraction of the microgel spheres in the AFM sample. Despite this discrepancy, the data presented by the AFM is consistent to the polymer swelling tendencies of the data presented by Curtis *et. al*.

Other than size distribution difference, a noticeable change in the polymer matrix as the pH decreases is the overall shape of the micelles appear to lose their spherical nature and become more "marshmallow-like" in consistency. This is likely due to the hydrated nature of the polymer microgels. The calculation for the water retention of the polymer is demonstrated in Equation 3.1:

$$V = \frac{4}{3}\pi r^3 \tag{3.1}$$

where $V$ is the volume of the sphere and $r$ is the radius of the polymer microgel.

Decreasing the pH from ~8 to ~4 increases the amount of water retention by ~30 times. This would cause the microgels to increase in fluidity as the AFM tip comes in contact with the polymer surface, and the swollen nature of these microgels would also cause the organized matrix to become more disorganized as the pH decreases. The texture differences of the latex vs. the microgels can also be seen in **Figure 3.4** and **3.5**. This added texture to the microgels is also likely caused by the interaction between the AFM tip and the fluid-like polymer surface, providing an artifact in the AFM image of the sample. These images also show the differences in the depth of the samples. As the pH decreases from pH ≈ 8 to pH ≈ 4, the depth increases from ~61 nm to ~145 nm, which further shows the solvation of the sample in three dimensions.

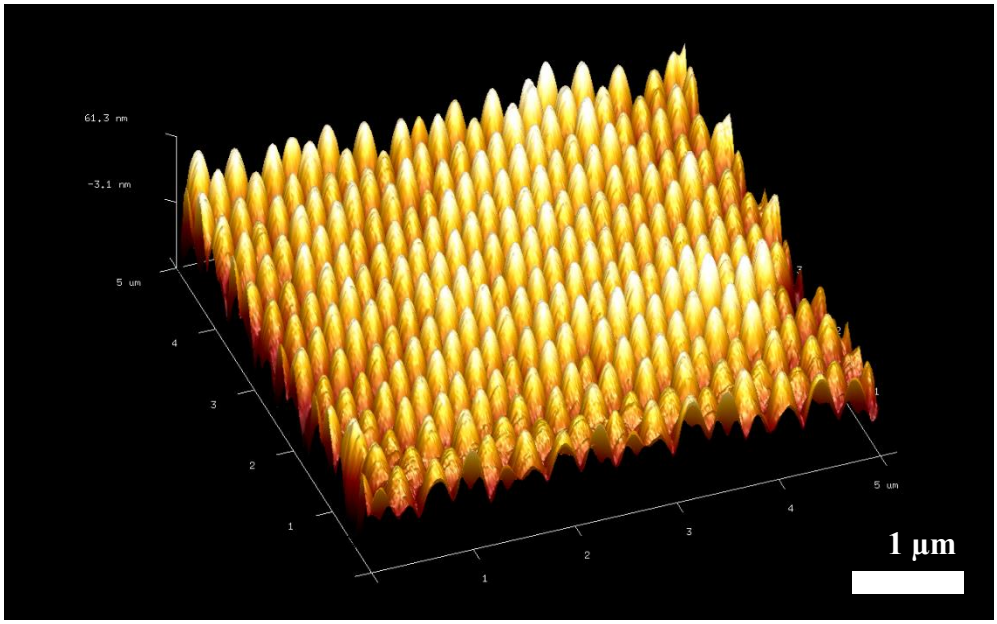


**Figure 3.4**. 3D AFM image of dehydrated $PS_{20}P2VP_{80}$ latex at pH ≈ 8. The scale bar is 1 µm.

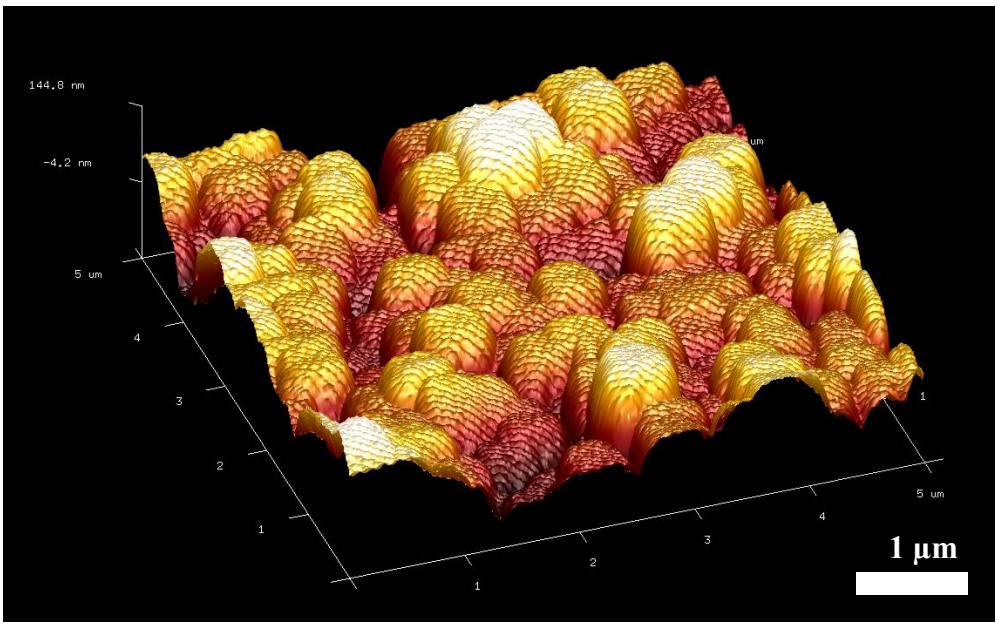


**Figure 3.5**. 3D AFM image of hydrated $PS_{20}P2VP_{80}$ latex at pH ≈ 4. The scale bar is 1 µm.

### 3.1.2 AuNP-$PS_{20}P2VP_{80}$ Particles

Au NPs with diameters of ~15 nm were successfully synthesized on the surface of the $PS_{20}P2VP_{80}$ random co-polymer utilizing a method outlined by Fales *et. al* and shown in the STEM image displayed in **Figure 3.6**.[2] The image shows homogeneous, monodispersed Au NPs reduced with dimethylamine borane (DMAB) to the surface of the $PS_{20}P2VP_{80}$ spheres with a calculated interparticle distance of ~10 nm. The concentration of AuNP-$PS_{20}P2VP_{80}$ is calculated at ~$10^9$ particles/mL due to the 3-fold dilution outlined in the methods.

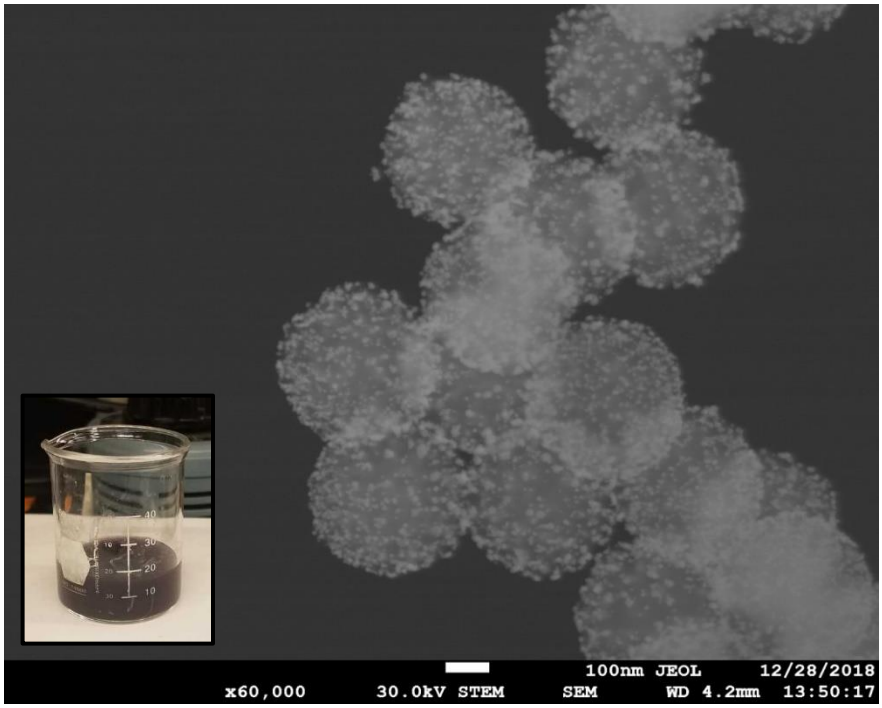


**Figure 3.6**. STEM image of AuNP-$PS_{20}P2VP_{80}$. The scale bar is 100 nm. Inset: Digital image of AuNP-$PS_{20}P2VP_{80}$ solution. Solution appeared purple in color upon reduction of $KAuCl_4$ with DMAB.

The UV-Vis extinction spectrum is shown in **Figure 3.7** with a SPR peak at 602 nm. The solution was diluted by a factor of 10× prior to acquiring the spectrum (~$10^8$ particles/mL) in order to match the concentrations of the Ag@AuNP-$PS_{20}P2VP_{80}$ and Au@AuNP-$PS_{20}P2VP_{80}$ solutions.

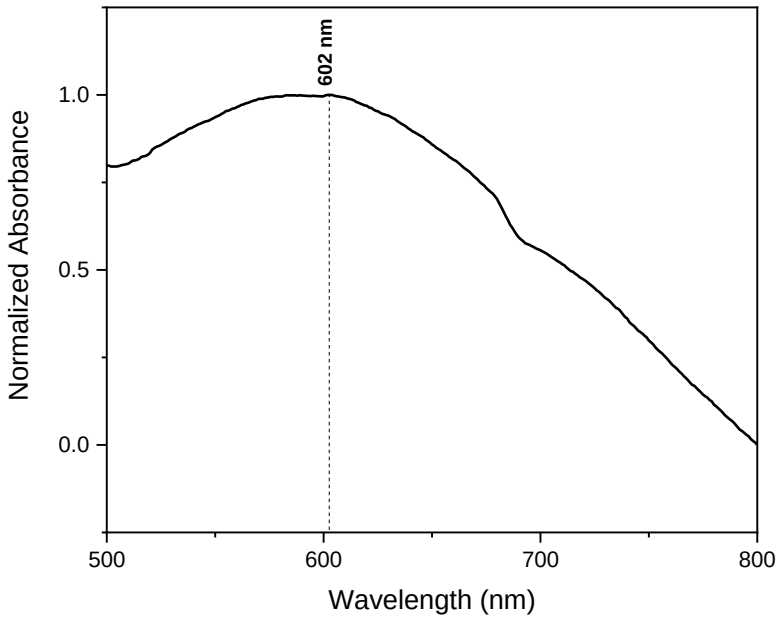


**Figure 3.7**. UV-Vis extinction spectrum of AuNP-$PS_{20}P2VP_{80}$.

### 3.1.3 Ag@AuNP-$PS_{20}P2VP_{80}$ Particles

Silver ions were successfully reduced on the surface of the AuNP-$PS_{20}P2VP_{80}$ to formulate ~25 nm Ag NPs on the microgel as shown in the STEM image displayed in **Figure 3.8**. The image shows homogeneous, monodispersed Ag NPs reduced with ascorbic acid and stabilized with sodium citrate. The Ag NPs on the surface of the $PS_{20}P2VP_{80}$ microgels have a calculated interparticle distance of ~5 nm. It should be noted that there appeared to be an excess of salt in the solution appearing in the center of the figure, which is likely due to an excess of sodium citrate.

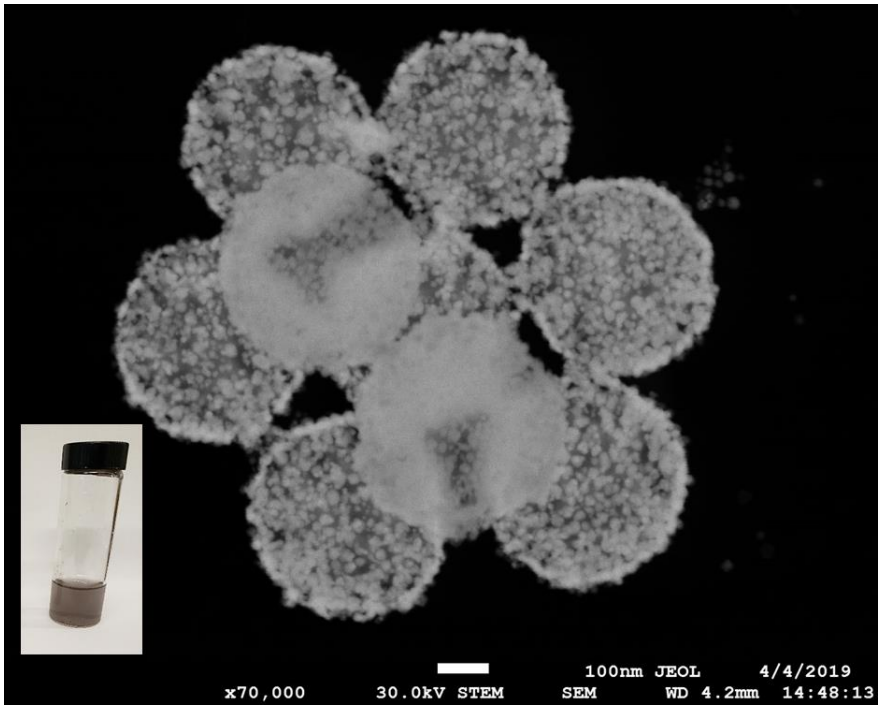


**Figure 3.8**. STEM image of Ag@AuNP-$PS_{20}P2VP_{80}$. The scale bar is 100 nm. Inset: Digital image of Ag@AuNP-$PS_{20}P2VP_{80}$ solution.

The EDS spectrum of the above sample is shown in **Figure 3.9** which shows the presence of both Ag and Au in the sample, consistent with an Au NP encapsulation in reduced Ag ions. It is important to note that the high concentration of Na in the system is likely from excess sodium citrate in the system, which is consistent with the salt seen in the STEM image. The existence of Cu and Al in the elemental composition of the sample is likely caused by background signaling from the copper TEM grids and is not from the NPs themselves. The existence of K and Cl in the system is from the reduction of the Au NP seeds with DMAB prior to the further reduction of Ag. The UV-Vis extinction spectra of the AuNP-$PS_{20}P2VP_{80}$ compared to both samples of Au@AuNP-$PS_{20}P2VP_{80}$ is shown in **Figure 3.10** with the SPR peak at 410 nm for the 25 nm Ag NPs.

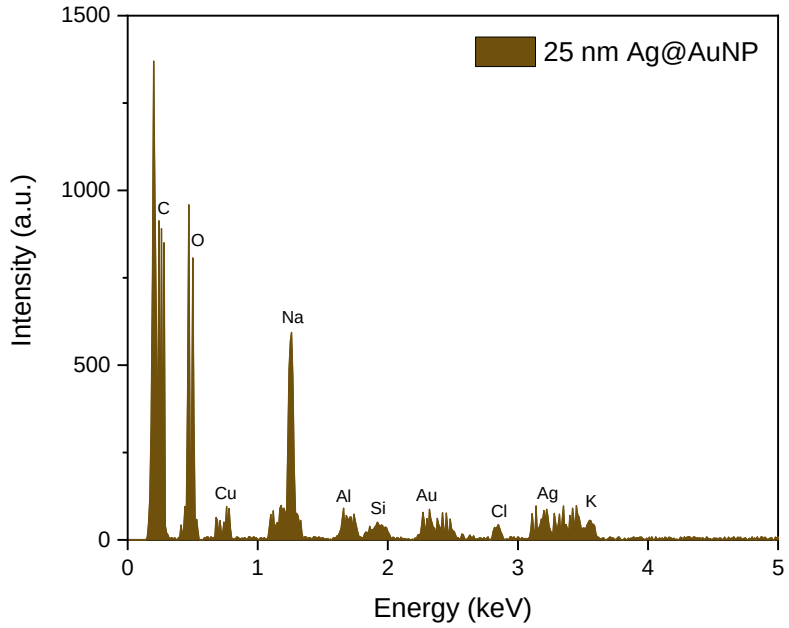


**Figure 3.8**. EDS spectrum of Ag@AuNP-$PS_{20}P2VP_{80}$.

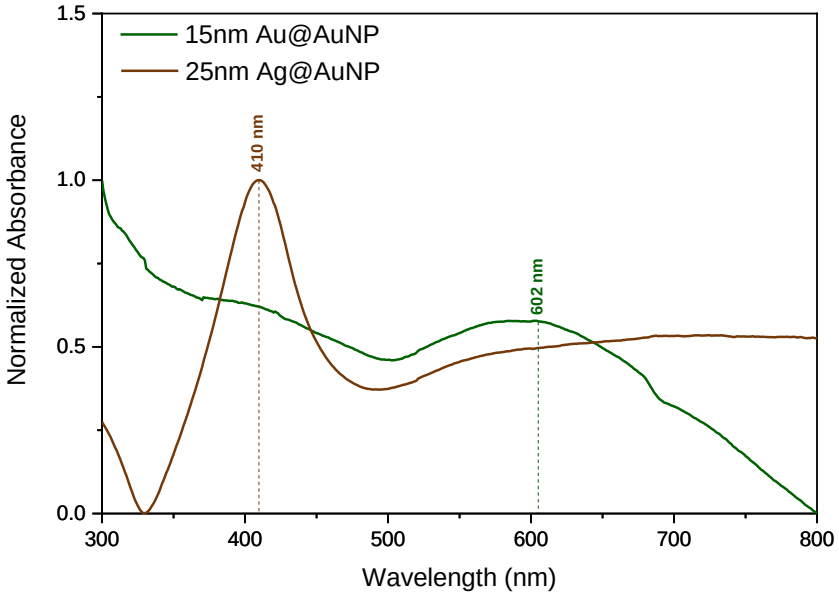


**Figure 3.10**. UV-Vis extinction spectra of AuNP-$PS_{20}P2VP_{80}$ and Ag@AuNP-$PS_{20}P2VP_{80}$.

### 3.1.4 Au@AuNP-$PS_{20}P2VP_{80}$ Particles

Gold ions were successfully reduced on the surface of the AuNP-$PS_{20}P2VP_{80}$ to formulate ~20 nm and ~35 nm Au NPs on the microgel as shown in the STEM images displayed in **Figure 3.11**. The images show homogeneous, monodispersed Au NPs reduced with hydroxylamine hydrochloride and stabilized with sodium citrate. The 20 nm Au NPs on the surface of the $PS_{20}P2VP_{80}$ microgels have a calculated interparticle distance of ~5 nm and the 35 nm Au NPs have a calculated interparticle distance of ~0.5 nm.

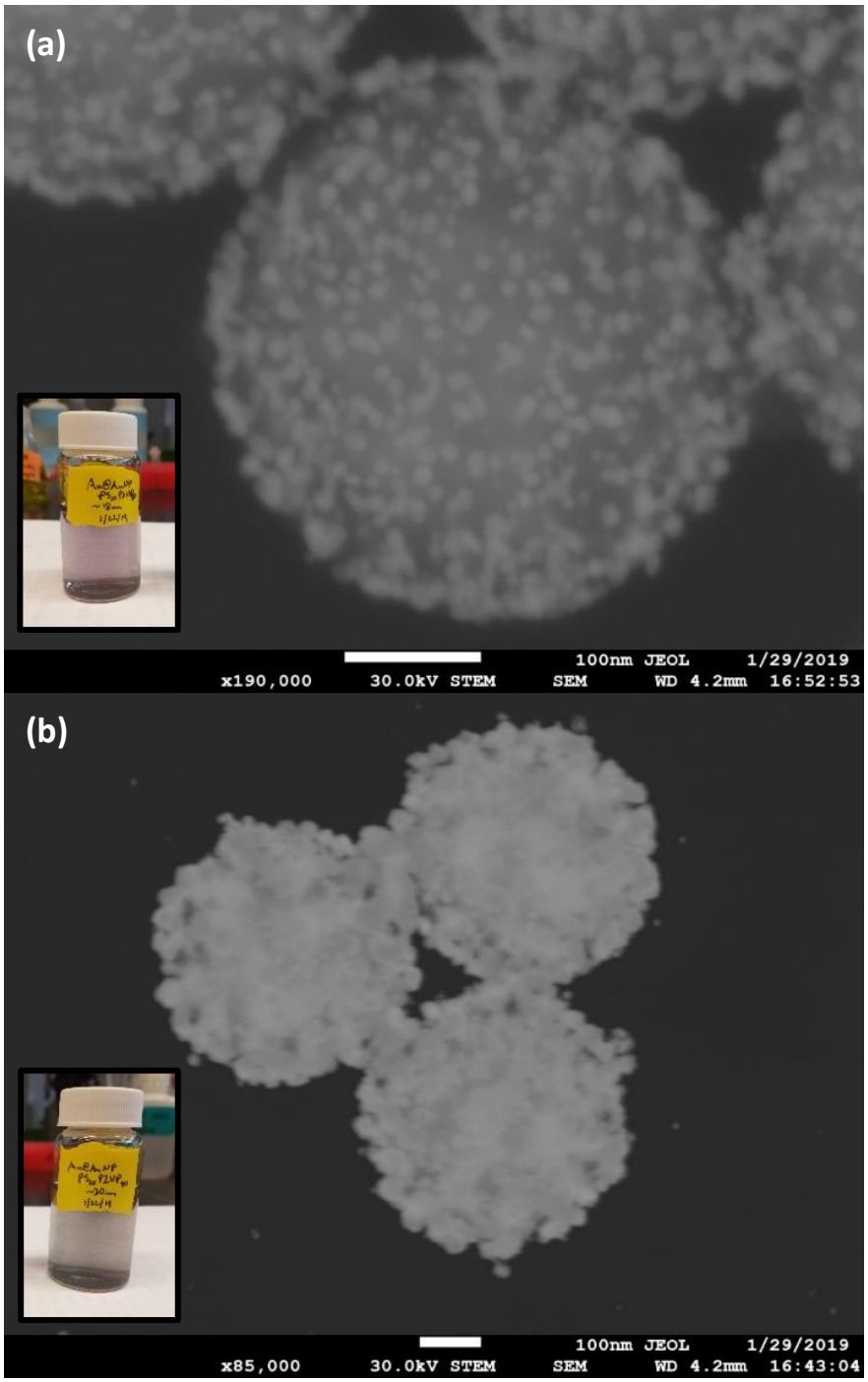


**Figure 3.11**. STEM image of Au@AuNP-$PS_{20}P2VP_{80}$ with NP measurements at (a) 20 nm and (b) 35 nm. The scale bars are 100 nm. Inset: Digital images of Au@AuNP-$PS_{20}P2VP_{80}$ solutions. The 20 nm Au NP solution appeared red-purple in color and the 35 nm Au NP solution appeared blue-purple in color.

The EDS data for the 35 nm Au@AuNP-$PS_{20}P2VP_{80}$ is recorded and shown in **Figure 3.12**, clearly indicating the presence of Au in the sample. The same chemicals were used to synthesize both the 20 nm and 35 nm Au@AuNP-$PS_{20}P2VP_{80}$, so it can therefore be assumed that the elemental compositions for both samples are identical.

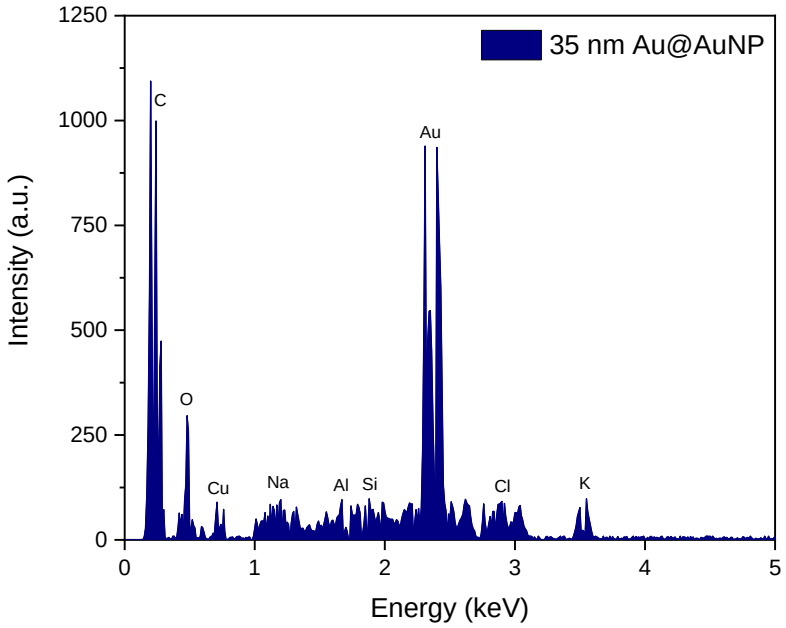


**Figure 3.12**. EDS spectrum of Au@AuNP-$PS_{20}P2VP_{80}$.

The UV-Vis extinction spectra of the AuNP-$PS_{20}P2VP_{80}$ compared to both samples of Au@AuNP-$PS_{20}P2VP_{80}$ is shown in **Figure 3.13** with SPR peaks at 646 nm for the 20 nm Au NPs and 678 nm for the 35 nm Au NPs. The wavelengths for the grating change for the spectra were at 300 nm and 900 nm. Note that with the 35 nm Au@AuNP-$PS_{20}P2VP_{80}$ sample, there appears to be multiple peaks shifted to 741 nm and 790 nm. This is likely caused by dipole and quadrupole excitations in the SPR of the coupled plasmonic Au NPs due to the small interparticle distance of these Au NPs on the surface of the polymer micelles.[3-6]

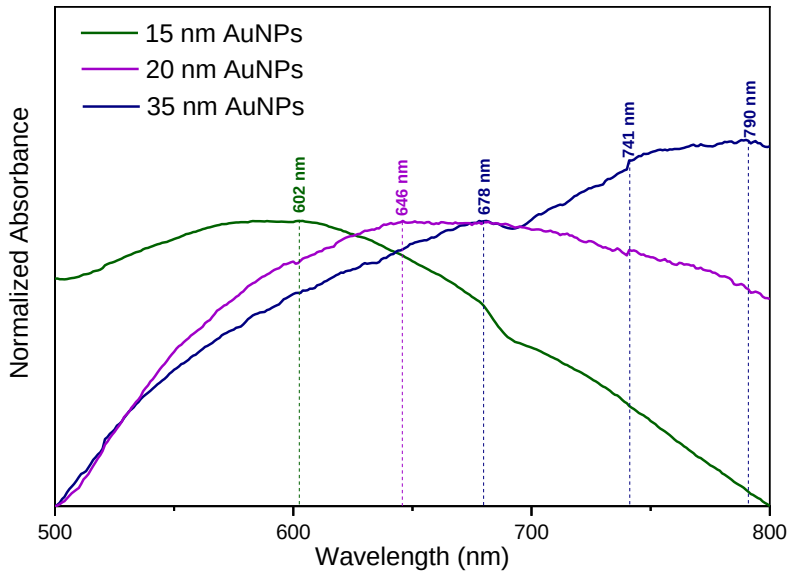


**Figure 3.13**. UV-Vis extinction spectra of AuNP-$PS_{20}P2VP_{80}$ and Au@AuNP-$PS_{20}P2VP_{80}$.

To ensure that a gold cage or shell had not formed around the microgels in the 35 nm Au@AuNP-$PS_{20}P2VP_{80}$, pH cycling experiments were completed via UV-Vis by adjusting the sample between pH ≈ 4 and pH ≈ 8 for 5 complete cycles as shown in **Figure 3.14**. The data shows that the absorbance wavelength consistently alternates between 550 nm at pH ≈ 4 and 610 nm at pH ≈ 8. This shows that the co-polymer is not constricted from swelling and contracting by the Au NPs on the surface, indicating that the polymer had not been encapsulated in a gold shell.

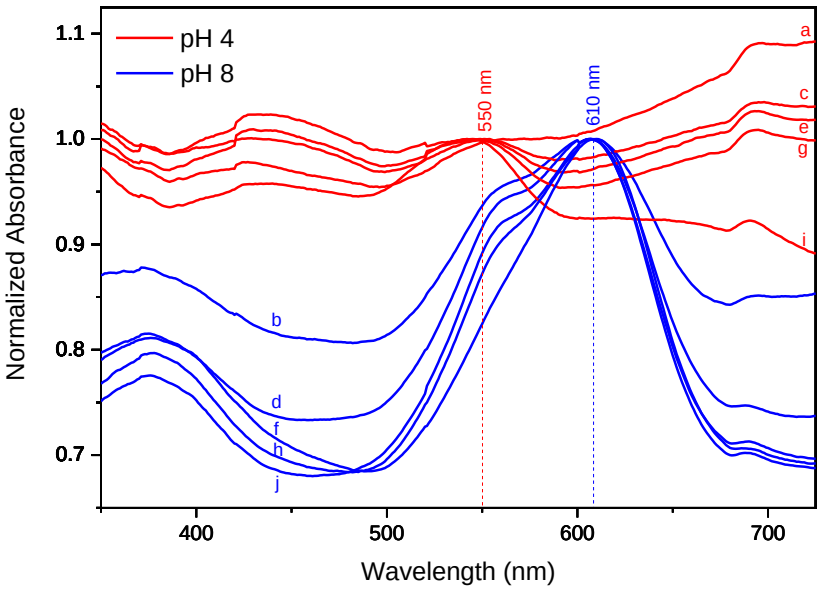


**Figure 3.14**. UV-Vis extinction spectra of Au@AuNP-$PS_{20}P2VP_{80}$ at altering pH measurements. The order of the cycles are labeled alphabetically (a – j).

## 3.2 Bulk SERRS Analysis

Reported are the results of the bulk surface-enhanced Raman scattering (SERS) analysis using CV as a reporter molecule to provide surface-enhanced resonance Raman scattering (SERRS). The structure of CV can be seen in **Figure 3.15**. CV is a molecule with high resonance that provides further enhancement of Raman signals below pH ≈ 9 when excited at 633 nm.[7] A Raman spectrum of CV is shown in **Figure 3.16** with a signal-to-noise (S/N) measurement of ~6.5,

which is below the quantitation limit of 10. In previous studies, the large resonance of CV has made it useful in SERRS analyses, producing multiple Stokes shift peaks when bound to a metal surface. The peak located at ~1620 $cm^{-1}$ was used for all S/N measurements for AuNP-$PS_{20}P2VP_{80}$ and Au@AuNP-$PS_{20}P2VP_{80}$. All spectra were obtained using a 633 nm laser light source and 60 s integration time.

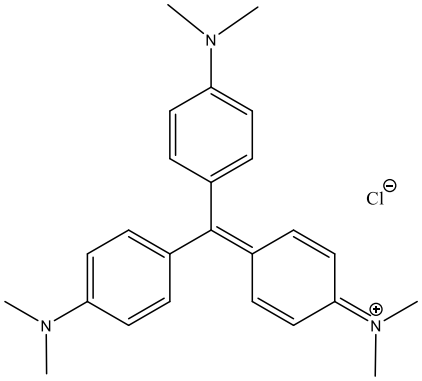


**Figure 3.15**. Chemical structure of crystal violet in solution.

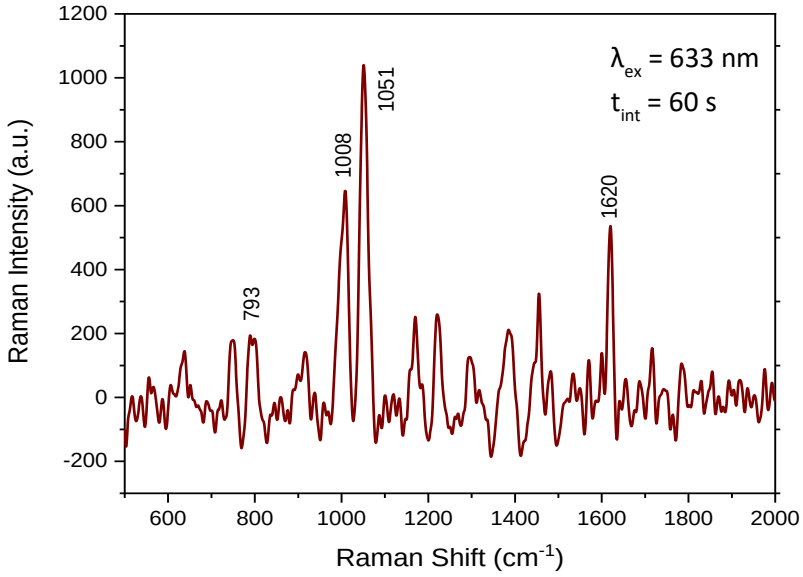


**Figure 3.16**. Bulk Raman spectrum of crystal violet in solution. [CV] = 9.26 M; $\lambda_{ex}$ = 633 nm; $t_{int}$ = 60 s.

### 3.2.1 Bulk SERRS Analysis with Crystal Violet Reporter Molecule

Bulk SERRS analyses of AuNP-$PS_{20}P2VP_{80}$ and Au@AuNP-$PS_{20}P2VP_{80}$ were successfully completed using CV as a reporter molecule. The solution concentration of CV for AuNP-$PS_{20}P2VP_{80}$, Ag@AuNP-$PS_{20}P2VP_{80}$ and Au@AuNP-$PS_{20}P2VP_{80}$ was 1.11 x $10^{-8}$ M. **Figure 3.17** and **3.18** show the SERRS spectra for each solution under neutral conditions (pH ≈ 6). A notable difference between each spectrum is the Raman peak intensity increases with the increasing metal NP size on the surface of the microgels, and the noise located in the range of 600 – 1100 $cm^{-1}$ decreases with the further enhancement. However, with the Ag NPs, the peak intensity increase is not significant enough in order to increase the S/N measurements of the system, and the excess citrate in the system provided a buffer to the solution to prevent significant pH changes. Therefore, further work is needed in order to fine-tune the ratios of the system in order to make the Ag@AuNP-$PS_{20}P2VP_{80}$ a viable SERS-active, pH-tunable substrate.

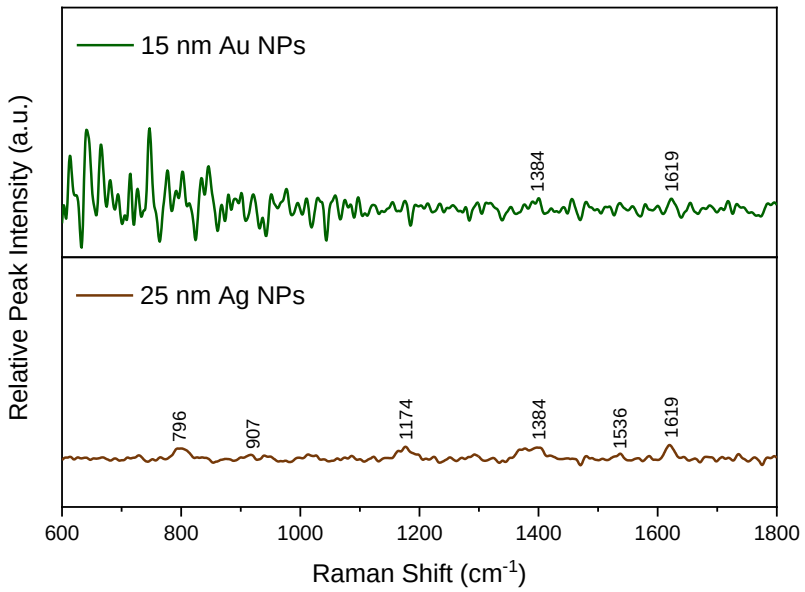


**Figure 3.17**. Bulk SERRS spectra of AuNP-$PS_{20}P2VP_{80}$ and Ag@AuNP-$PS_{20}P2VP_{80}$. $\lambda_{ex}$ = 633 nm; $t_{int}$ = 60 s.

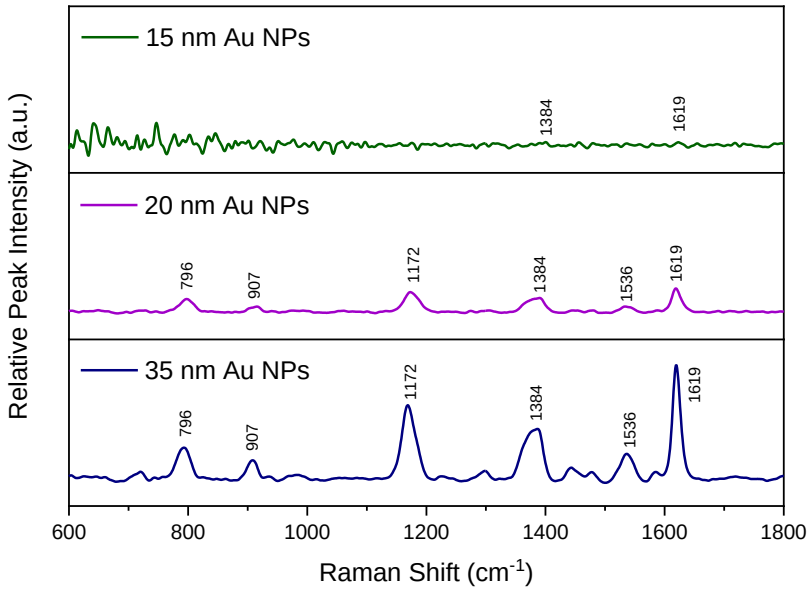


**Figure 3.18**. Bulk SERRS spectra of AuNP-$PS_{20}P2VP_{80}$ and Au@AuNP-$PS_{20}P2VP_{80}$. $\lambda_{ex}$ = 633 nm; $t_{int}$ = 60 s.

The S/N measurements for the Au NP solutions, shown in **Figure 3.19**, also indicate a direct linear relationship between NP size and peak intensity. The AuNP-$PS_{20}P2VP_{80}$ solution has a S/N measurement of ~11, which is just above the quantitation limit. The 20 nm Au@AuNP-$PS_{20}P2VP_{80}$ solution has a S/N measurement of ~85 and the 35 nm Au@AuNP-$PS_{20}P2VP_{80}$ solution has a S/N measurement of ~250. Due to this drastic increase of the SERRS S/N measurement, all following analyses were completed focusing on the 35 nm Au@AuNP-$PS_{20}P2VP_{80}$ solution.

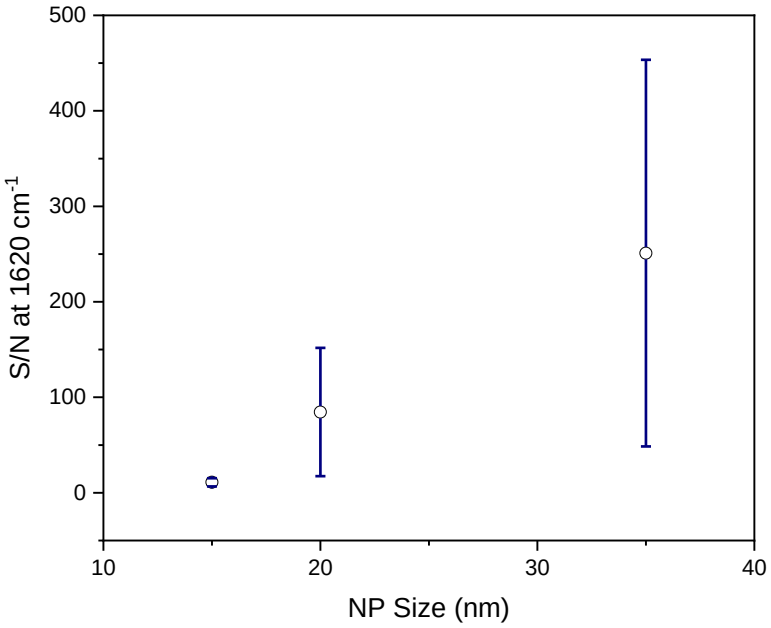


**Figure 3.19**. Bulk SERRS S/N measurements of AuNP-$PS_{20}P2VP_{80}$ and Au@AuNP-$PS_{20}P2VP_{80}$ comparing NP size.

### 3.2.2 Bulk SERRS Analysis with Alternating pH

A pH cycling analysis was completed for the 35 nm Au@AuNP-$PS_{20}P2VP_{80}$ solution to adjust the polymer micelles from a microgel to a latex form in order to test the stability of the NP-polymer system. **Figure 3.20** shows the SERRS spectra for the 35 nm Au@AuNP-$PS_{20}P2VP_{80}$ at pH ≈ 4 and pH ≈ 6. It is well noted that the Raman peak intensity of the acidic solution decreases as the polymer swells, increasing the interparticle distance between the Au NPs. At pH ≈ 4 the polymer diameter is measured at ~720 nm via AFM. Therefore the calculated interparticle distance

of the 35 nm Au@AuNP-$PS_{20}P2VP_{80}$ system increased from ~0.5 nm at neutral conditions to ~60 nm under acidic conditions.

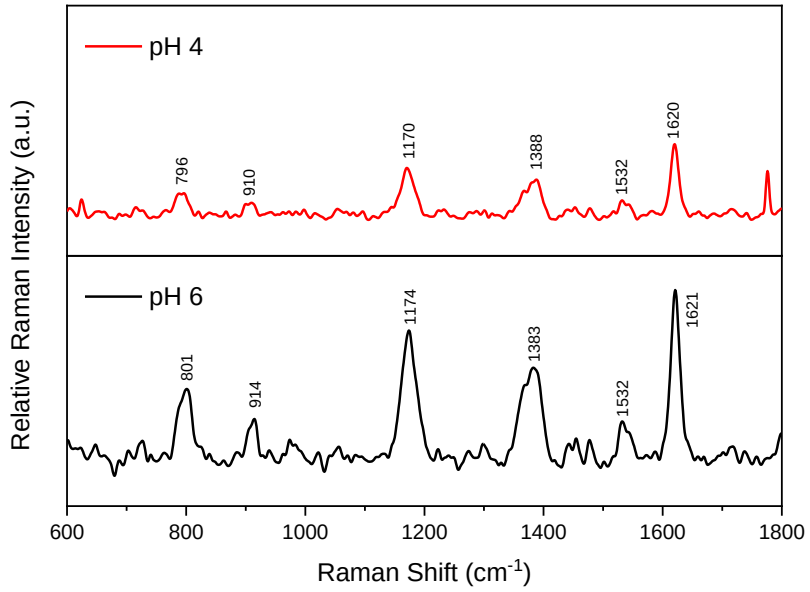


**Figure 3.20**. Bulk SERRS spectra of 35 nm Au@AuNP-$PS_{20}P2VP_{80}$ at altering pH. $\lambda_{ex}$ = 633 nm; $t_{int}$ = 60 s.

**Figure 3.21** shows the pH cycling S/N measurements of 35 nm Au@AuNP-$PS_{20}P2VP_{80}$ where the half-cycle measurements correspond to pH ≈ 4 conditions and full-cycle measurements correspond to pH ≈ 6 conditions. It is important to note that the S/N measurements for one complete cycle of pH adjustments drops from an original S/N ratio of ~250 to ~65. This is likely caused by the added salt in solution producing an increased background signal. However, the added salt in solution increases the ionic strength of the polymer network and is likely better for screening changes.[1] Therefore, the higher concentration of ions in the solution would favor improvements in the swelling and contracting ratios of the polymer microspheres, which is consistent with the cycling graph. The graph shows that the solution is stable with continued pH adjustments alternating between S/N measurements of 23 – 47 at pH ≈ 4 and S/N measurements

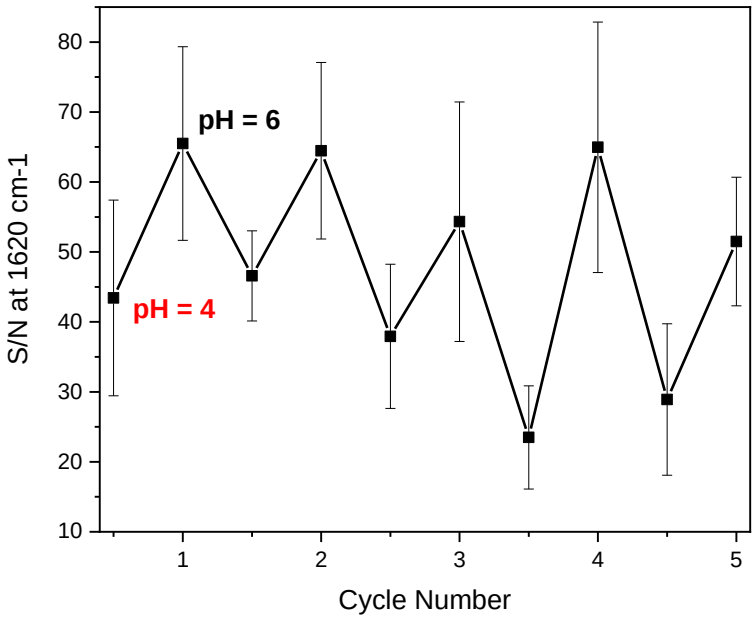


**Figure 3.21**. Bulk SERRS S/N measurements of 35 nm Au@AuNP-$PS_{20}P2VP_{80}$ at altering pH.

of 51 – 65 at pH ≈ 6, and these ratios improve with increasing additions of acid and base. The large standard deviation of the data is caused by tendency of the particles to settle out of solution over time. This settling is likely due to the large mass of the particles and can be controlled by decreasing the size of the polymer microgels. This will be explored in future research.

## 3.3 Single-Particle SERRS Analysis

Reported are the results of the single-particle SERRS analysis of 35 nm Au@AuNP-$PS_{20}P2VP_{80}$ using CV as a reporter molecule. A Raman spectrum for CV on the single-particle microscope is shown in **Figure 3.22** with a calculated S/N ratio of ~14. For all spectra obtained, a 633 nm HeNe laser was used with a manually adjusted spot size of 500 nm in order to analyze a single particle on the surface of the sample slide. All spectra were obtained using an integration

time of 5 s and a laser power of ~9 µW to avoid photo bleaching and photo degradation of the sample.

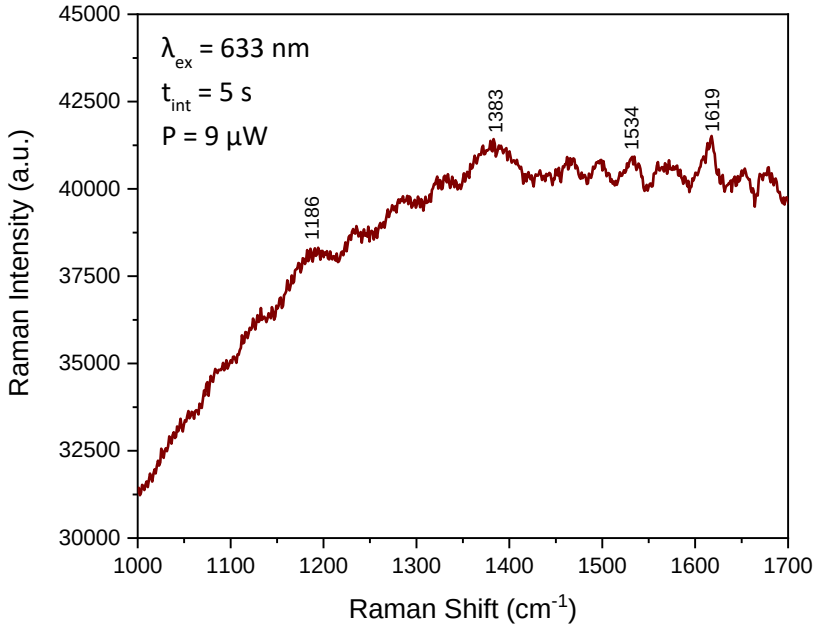


**Figure 3.22**. Single-particle Raman spectrum of crystal violet in solution. [CV] = 9.26 M. $\lambda_{ex}$ = 633 nm; $t_{int}$ = 5 s; P = 9 µW.

### 3.3.1 Single-Particle SERRS Analysis with Crystal Violet Reporter Molecule

A single-particle SERRS analysis of 35 nm Au@ AuNP-$PS_{20}P2VP_{80}$ was successfully completed using CV as a reporter molecule. **Figure 3.23** shows a SERRS spectrum of a single NP-polymer particle. This strong signal has also shown to be stable over an extended period of time, as shown in **Figure 3.24**. It is important to note that the peak signals do not shift in wavenumber over time, which would indicate the presence of photodegradation, and the major peaks located at 1171 $cm^{-1}$, 1367 $cm^{-1}$, 1388 $cm^{-1}$ and 1615 $cm^{-1}$ remain fairly constant in intensity for the duration. The calculated S/N ratio for the single-particle SERRS data is ~335 which is comparable to that

of the bulk SERRS data. The increase of the S/N ratio with the single-particle SERRS data is likely due to a lack of solvent on the sample slide, decreasing the background signal of the sample.

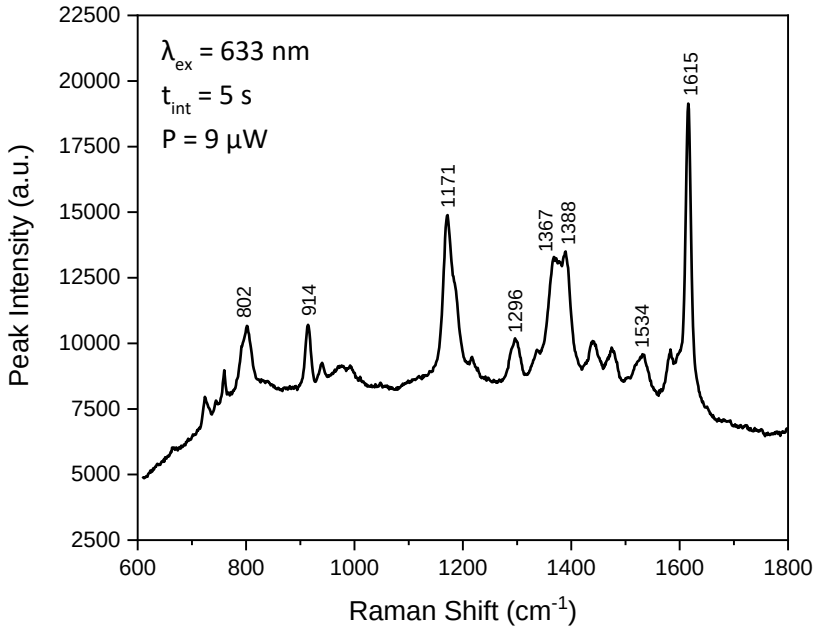


**Figure 3.23**. Single-particle SERRS spectrum of 35 nm Au@AuNP-$PS_{20}P2VP_{80}$. $\lambda_{ex}$ = 633 nm; $t_{int}$ = 5 s; P = 9 µW.

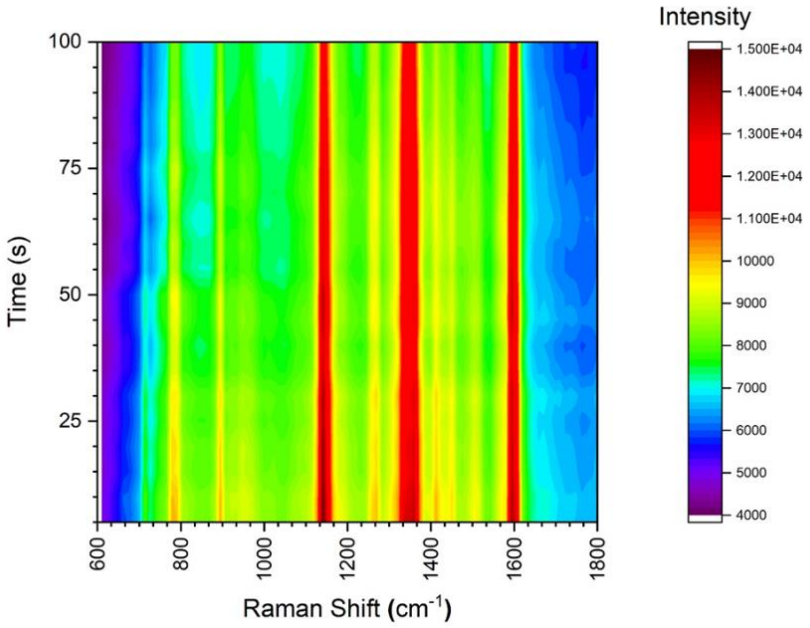


**Figure 3.24**. Single-particle SERRS spectra intensity map of 35 nm Au@AuNP-$PS_{20}P2VP_{80}$ over time. $t_{int}$ = 5 s and P = 9 µW laser.

### 3.3.2 Single-Particle SERRS Analysis with Alternating pH

A pH cycling analysis was completed for the 35 nm Au@AuNP-$PS_{20}P2VP_{80}$ sample to adjust the polymer from microgel to latex form and compare the S/N ratio to that of the bulk SERRS analysis. Since the dried sample under neutral conditions (pH ≈ 6) showed an increased S/N ratio than that of the aqueous bulk sample under the same conditions, it was anticipated that the S/N cycling ratios would show the same trend. **Figure 3.25** shows the SERRS spectra of 35 nm Au@AuNP-$PS_{20}P2VP_{80}$ under acidic conditions (pH ≈ 4) and basic conditions (pH ≈ 8).

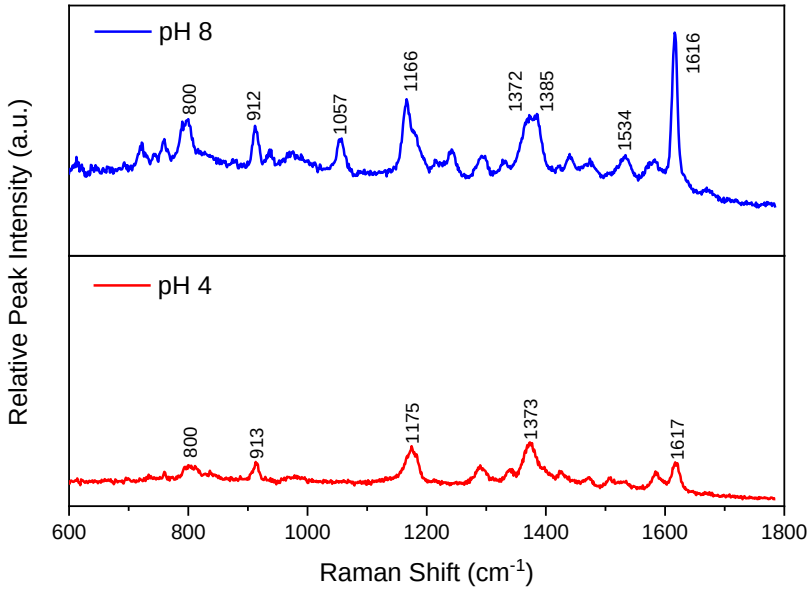


**Figure 3.25**. Single-particle SERRS spectra of 35 nm Au@AuNP-$PS_{20}P2VP_{80}$ at altering pH. $\lambda_{ex}$ = 633 nm; $t_{int}$ = 5 s; P = 9 µW.

The sample was unable to be vortexed while on the sample slide because doing so would increase the risk of the particles detaching from the slide and becoming lost in the pipetting process. It was therefore decided to increase the basicity of the sample to pH ≈ 8 instead of pH ≈ 6 prior to obtaining spectra to ensure that the pyridine groups of the micelles were fully deprotonated. However, as described by Curtis *et. al*, the hydrophobic diameter of the micelles do not alter in significant quantities above pH ≈ 6.[1] Therefore, the interparticle distance of the Au NPs is still calculated as ~0.5 nm under both pH ≈ 6 and pH ≈ 8 conditions.

After 5 pH altering cycles for a single particle, the S/N ratios were calculated and are shown in **Figure 3.26** where each half-cycle measurement corresponds to spectra obtained at pH ≈ 4 and full-cycle measurements correspond to spectra obtained at pH ≈ 8. This figure shows a similar cycling trend to that of the bulk SERRS analysis and proves sample stability. However, it should be noted that the S/N ratios of the single-particle SERRS analysis alternates between S/N measurements of 95 – 131 at pH ≈ 4 to 120 – 180 at pH ≈ 8, which is over 3 times greater than that of the bulk SERRS analysis due to the lack of solvent in the sample. It is also noted that the

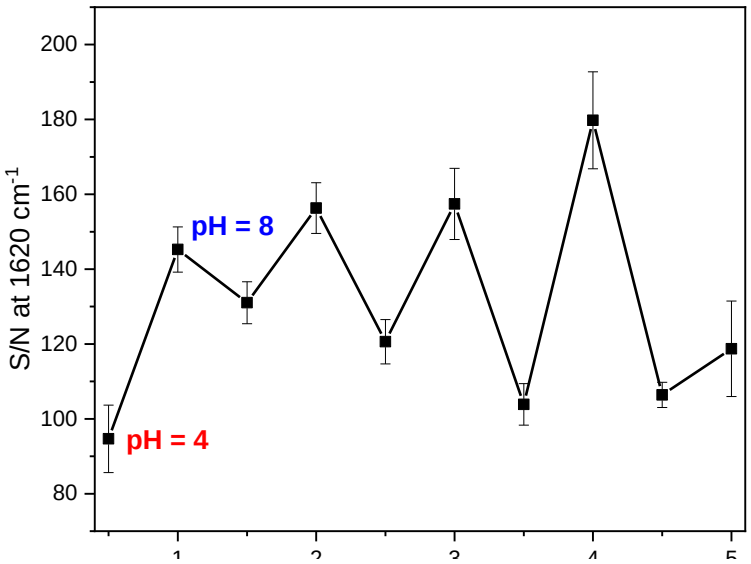


**Figure 3.26**. Single-particle SERRS S/N measurements of 35 nm Au@AuNP-$PS_{20}P2VP_{80}$ at altering pH.

standard deviation of the data is less than that of the bulk SERRS data because the particles were adhered to a solid surface prior to obtaining spectra, which minimizes error caused by particles settling out of solution. Lastly, the data shows a similar trend to that of the bulk data where the increasing ionic strength of the sample allows for further stability of the microgel swelling ratios with each acid/base titration.

This experiment was repeated for 3 different particles and the S/N ratios for each particle were calculated and shown in **Figure 3.27**. This figure shows that a similar cycling trend can be seen in all 3 particles, which proves sample reproducibility. The average S/N ratios for all 3 particles were also calculated and are shown in **Figure 3.28**, which shows the average S/N ratios alternating between S/N measurements of 126 – 152 at pH ≈ 4 and 162 – 196 at pH ≈ 8, which is over 3 times greater than that of the bulk SERRS S/N measurements.

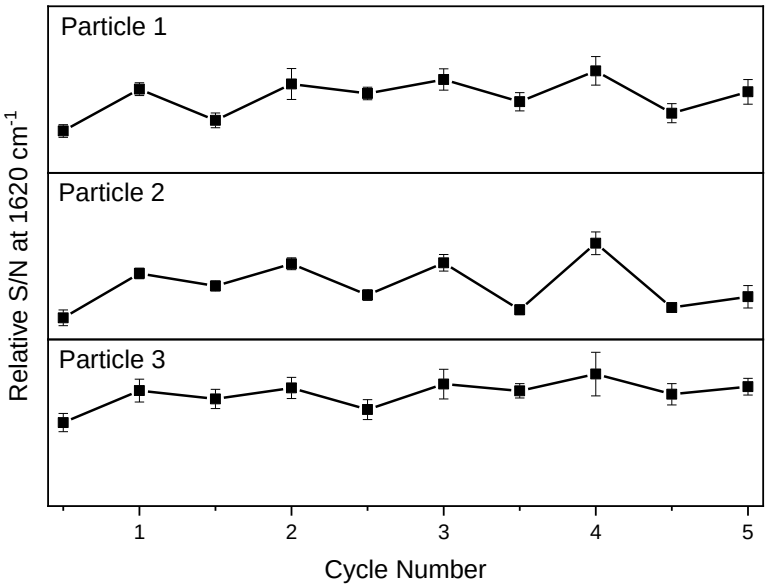


**Figure 3.27**. Single-particle SERRS S/N measurements of 35 nm Au@AuNP-$PS_{20}P2VP_{80}$ at altering pH for 3 different particles.

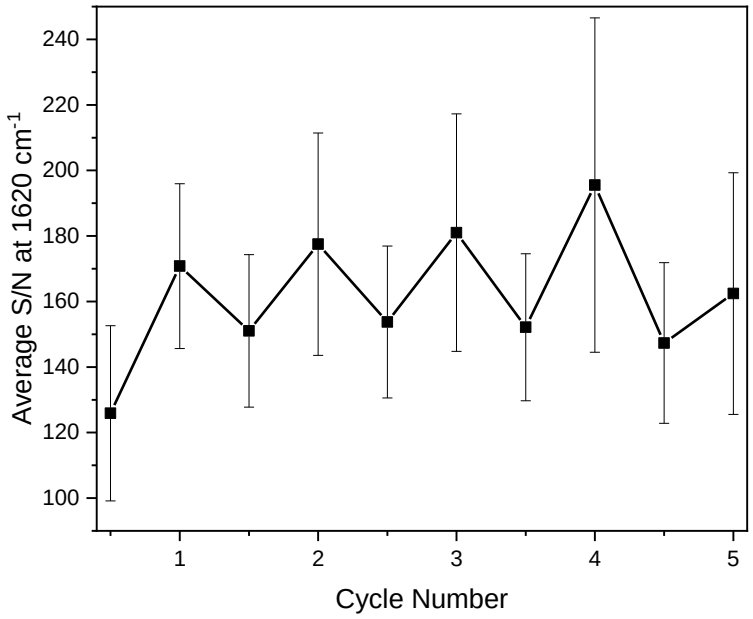


**Figure 3.28**. Average single-particle SERRS S/N measurements of 35 nm Au@AuNP-$PS_{20}P2VP_{80}$ at altering pH for 3 different particles.

To further compare the single-particle SERRS data with that of the bulk SERRS data, the analytical enhancement factors (AEFs) for all NP SERRS peak in intensities in comparison to the peak intensities for the cyclohexane standard were calculated and shown in **Table 3.1**. The calculations conclude that the AEF values increase with the increasing Au NP size on the surface of the polymer micelles for bulk SERRS. Also, for the 35 nm AuNP-$PS_{20}P2VP_{80}$ sample, the single-particle SERRS spectra at an integration of 5 s have an AEF that is over double the value to the bulk SERRS spectra at an integration of 60 s due to the increased sensitivity and decreased spot size of the single-particle Raman instrumentation.

**Table 3.1.** Summary of calculated analytical enhancement factors for the 1620 $cm^{-1}$ Raman active mode of CV.

| Raman Instrument | Sample | Integration Time (s) | Analytical Enhancement Factor (AEF) |
|---|---|---|---|
| **Bulk** (Delta Nu) | 15 nm AuNP-$PS_{20}P2VP_{80}$ | 60 | $1.21 \times 10^{7}$ |
| | 25 nm Ag@AuNP-$PS_{20}P2VP_{80}$ | 60 | $1.37 \times 10^{7}$ |
| | 20 nm Au@AuNP-$PS_{20}P2VP_{80}$ | 60 | $1.42 \times 10^{10}$ |
| | 35 nm Au@AuNP-$PS_{20}P2VP_{80}$ | 60 | $2.44 \times 10^{10}$ |
| **Single-Particle** (Olympus) | 35 nm Au@AuNP-$PS_{20}P2VP_{80}$ | 5 | $5.01 \times 10^{10}$ |

## 3.4 Conclusions and Future Directions

A SERS-active substrate composed of size-tunable Au NPs and $PS_{20}P2VP_{80}$ polymer latex was successfully synthesized. STEM images show a high density of Au NPs on the surface of the micelles producing an interparticle distance measurement as low as 0.5 nm between Au NPs. The polymeric swelling was demonstrated via AFM, UV-Vis and SERRS with high stability and reproducibility over time, and the interparticle distance between Au NPs proved to be tunable and stable over extended pH cycles. SERRS measurements were successfully obtained for both bulk SERS and single-particle SERS instrumentation with high S/N ratios and AEF values above $10^{10}$.

Future directions with this Au NP-Polymer system include further studies of reducing silver ions onto the AuNP-$PS_{20}P2VP_{80}$ system to formulate a SERS-active substrate capable of responding to pH changes. This will involve fine-tuning the ratios of sodium citrate to the particles in order to stabilize the system while minimizing the formulation of a buffer. Extended work will involve altering the hydrodynamic diameter of the polymer micelles to 50 – 150 nm for the purpose of increasing solution stability and increasing permeability of the particles through cellular membranes. This can be achieved by altering the quantity of initiator and changing the surfactant to one that decreases the surface tension of the micelles. Combining these alterations with sonication will be explored as well as changing the initiator to one that is UV light-reactive. Lastly, the encapsulation of quantum dots or magnetite into the polymer micelles will enhance the multifunctionality of these microgels by improving the purification of the NP-polymer particles as well as increase the instrumentation methods to which these particles can be characterized. Iron NPs can allow for selective purification via magnetism while quantum dots can allow for tracking via fluorescence while being protected from aggregation or quenching by the polymer beads. In particular, adjusting the polymer size and adding quantum dots can allow for tracking the particles in a biological system and even map pH changes within cellular membranes. This is a direction that is hoped to be explored further as instrumentation improves.

## References

1. Curtis, T.; Taylor, A. K.; Alden, S. E.; Swanson, C.; Lo, J.; Knight, L.; Silva, A.; Gates, B. D.; Emory, S. R.; Rider, D. A. Synthesis and Characterization of Tunable, pH-Responsive Nanoparticle–Microgel Composites for Surface-Enhanced Raman Scattering Detection. *ACS Omega*. **2018**, *3*, 10572-10588.
2. Fales, A. M.; Yuan, H.; Vo-Dinh, T. Development of Hybrid Silver-Coated Gold Nanostars for Nonaggregated Surface-Enhanced Raman Scattering. *J. of Phys. Chem. C*, **2014**, *118*, 3708-3715.

3. Chen, F.; Alemu, N.; Johnston, R. L. Collective plasmon modes in a compositionally asymmetric nanoparticle dimer. *AIP Adv. 1*. **2011**, *1* (032134), 1-16.
4. Zhou, F.; Li, Z.-Y.; Liu, Y. Quantitative Analysis of Dipole and Quadrupole Excitation in the Surface Plasmon Resonance of Metal Nanoparticles. *J. Phys. Chem. C* **2008**, *112*, 20233-20240.
5. Clarkson, J. P.; Winans, J.; Fauchet, P. M. On the scaling behavior of dipole and quadrupole modes in coupled plasmonic nanoparticle pairs. *Optic. Mater. Exp.* **2011**, *1* (5), 970-979.
6. Babicheva, V. E. and Evylukhin, A. B. Electric quadrupole and magnetic dipole coupling in plasmonic nanoparticle arrays. *ACS Photonics* **2018**, *5* (5), 1-11.
7. Adak, A.; Bandyopadhyay, M.; Pal, A. Removal of crystal violet dye from wastewater by surfactant-modified alumina. *Sep. and Purif. Technol.* **2005**, *44* (2), 139-144.